

# Massive loops in thermal SU(2) Yang-Mills theory: Radiative corrections to the pressure beyond two loops

Ingolf Bischer<sup>†</sup>, Thierry Grandou<sup>\*</sup>, and Ralf Hofmann<sup>†</sup>

<sup>\*</sup> Université Cote d'Azur,  
Institut de Physique de Nice,  
Routes des Lucioles, 06560 Valbonne, France

<sup>†</sup> Institut für Theoretische Physik,  
Universität Heidelberg,  
Philosophenweg 16, 69120 Heidelberg, Germany

## Abstract

We devise an efficient book-keeping of excluded energy-sign and scattering-channel combinations for the loop four-momenta associated with massive quasi-particles, circulating in (connected) bubble diagrams subject to vertex constraints inherited from the thermal ground state. The according radiative corrections modify the free thermal-quasiparticle pressure at one loop. Increasing the loop order in two-particle irreducible (2PI) bubble diagrams, we exemplarily demonstrate a suppressing effect of the vertex constraints on the number of valid combinations. This increasingly strong suppression gave rise to the conjecture in hep-th/0609033 that the loop expansion would terminate at a finite order. Albeit the low-temperature dependence of the 2PI 3-loop diagram complies with this behaviour, a thorough analysis of the high-temperature situation reveals that the leading power in temperature is thirteen such that this diagram dominates all lower loop orders for sufficiently high temperatures. An all-loop-order resummation of 2PI diagrams with dihedral symmetry is thus required, defining an extremely well-bounded analytical continuation of the low-temperatures result.

# Contents

<b>1</b>	<b>Introduction</b>	<b>1</b>
<b>2</b>	<b>Exclusion of sign configurations in massive bubble diagrams</b>	<b>3</b>
2.1	Exclusion tables . . . . .	4
2.2	Exclusions for 2PI pressure diagrams up to six loops . . . . .	5
2.2.1	Two-loop diagram . . . . .	5
2.2.2	2PI three-loop diagram . . . . .	6
2.2.3	2PI four-loop diagram . . . . .	7
2.2.4	The two 2PI five-loop diagrams . . . . .	10
2.2.5	The four 2PI six-loop diagrams . . . . .	11
2.2.6	Summary of results up to six loops . . . . .	11
2.3	Finiteness of $R$ at any finite loop order . . . . .	13
<b>3</b>	<b>Review of up to two-loop diagrams</b>	<b>15</b>
3.1	One-loop pressure . . . . .	15
3.2	Two-loop correction . . . . .	15
<b>4</b>	<b>The 2PI three-loop diagram</b>	<b>16</b>
4.1	Loop integral . . . . .	17
4.2	Properties of the vertex constraint . . . . .	18
4.3	High-temperature analysis . . . . .	20
4.4	Match of high- to low-temperature behaviour . . . . .	28
<b>5</b>	<b>Resummation of two-particle irreducible diagrams with dihedral symmetry</b>	<b>31</b>
<b>6</b>	<b>Summary, Conclusions, and Outlook</b>	<b>34</b>
<b>A</b>	<b>Derivation of equation (42)</b>	<b>35</b>

## 1 Introduction

Four dimensional Yang-Mills thermodynamics is a fascinating subject [1]. However, attempts to tackle the high-temperature Yang-Mills problem in terms of small-coupling expansions [2–8] lead to a poorly controlled foliation [9] of (likely infinitely many) hierarchical momentum scales [10, 11]. The integration of this hierarchy presumably represents an unsurmountable technical difficulty and conceptually is questionable. The problems induced by the perturbative approach can be traced to the disregard of an appropriate deconfining thermal ground-state estimate which is composed of Yang-Mills field configurations that, as a matter of principle, are inaccessible to small-coupling expansion: Harrington-Shepard (anti)calorons [12] for SU(2) and SU(3) gauge groups [1]. In fact, propagating disturbances and quantum fluctuations as well as

their residual correlations are direct consequences of the excitability of this ground state [13]. Since already on the level of free excitations a part of the spectrum is represented by thermal quasiparticles due to an adjoint Higgs mechanism, since the ground state is associated with a scale of maximum resolution, and since there is a straightforward physical and completely fixed gauge, radiative corrections are void of infrared divergences, and the ultraviolet cutoff can be prescribed in a physically meaningful way. Recall that thermal perturbation theory requires a renormalisation programme which performs subtractions in certain, technically convenient gauges by appealing to zero-temperature renormalisation conditions [9, 14].

The usefulness of a deconfining thermal ground state as an a priori estimate would be reflected by the fact that radiative corrections to free quasiparticle excitations are in some sense hierarchically small. Therefore, it is of utmost importance to construct an accordingly exhaustive expansion scheme. A seemingly natural expansion of radiative corrections is in loop orders [15]. Note that such an expansion does not necessarily rely on the smallness of the coupling constant. In fact, the gauge coupling constant  $e$  of deconfining SU(2) Yang-Mills thermodynamics is  $e = \sqrt{8\pi} > 1$  for almost all possible temperatures [1]. In [16] all two-loop corrections to the pressure were computed, and, compared to the one-loop result, a hierarchical suppression was observed<sup>1</sup>.

In the present work we investigate whether such a hierarchical suppression with increasing but fixed loop order holds beyond two loops. To keep the technical complexity at a minimum, we consider loop diagrams that exclusively involve massive quasiparticles since these are characterised by thermal fluctuations only [1]. In spite of the fact that the ratio of allowed energy-sign and scattering-channel combinations to such a priori possible combinations decreases with increasing loop order, we find that, starting at the 2PI three-loop order, the hierarchical suppression is spoiled for temperatures  $T$  sufficiently far above the critical temperature  $T_c$  of the deconfining-preconfining phase transition. This calls for a resummation within a certain class of all-order 2PI loop diagrams. Indeed, we demonstrate that such a resummation generates an analytic temperature dependence which is well bounded for all temperatures  $T \geq T_c$ .

This paper is organised as follows. In Sec. 2 we review the constraints on invariant momentum transfer through a 4-vertex involving massive modes only and, based on this, set up a counting scheme for excluded energy-sign and scattering-channel combinations. This scheme is subsequently applied to 2PI bubble diagrams up to six-loop order as they occur in the loop expansion of the pressure. We observe that the ratio  $R$  of allowed vs. a priori possible combinations monotonically decreases with increasing loop number. However, we also prove that within a class of dihedrally symmetric diagrams  $R$  never vanishes at any finite loop order and that therefore a more quantitative assessment of higher loop orders is required to judge their importance. In preparing such an assessment, we review bubble diagrams up to two-loop order in Sec. 3. In a next step, Sec. 4 and App. A address the computational intricacies one encounters in computing the 2PI three-loop diagram. Namely, we derive the expres-

---

<sup>1</sup>The three-loop results in [17] are erroneous due to the appeal to incorrect vertex constraints.

sion for the (six-dimensional) loop integral and investigate the vertex constraint to be able to set up a high-temperature treatment of this integral. While low temperatures can be subjected to the Monte-Carlo method, we are able to analytically extract the leading powers in the high-temperature situation for each possible scattering-channel combination (diagonal and off-diagonal): The diagonal case exhibits a leading-power thirteen temperature dependence while the off diagonal case contributes with maximal power four only. Compared to the high-temperature one-loop pressure there thus is a relative power of nine for the diagonal case which would ruin the idea of the thermal ground state and its free quasiparticle excitations to represent a useful a priori estimate if the loop expansion was to be truncated at order three. Fortunately, we had already shown in Sec. 2 that this is not the entire story since there are infinitely many dihedrally symmetric diagrams which enjoy a finite support in their loop integrations. In Sec. 5 we formally resum their contributions in terms of the according, truncated Dyson-Schwinger equation for the full 4-vertex. This yields an analytical continuation of the well-controlled low-temperature situation which turns out to be extremely well bounded. If the high-temperature form factor for the 4-vertex, as it is obtained from the Dyson-Schwinger treatment, is used to compute the leading temperature powers in two-loop and 2PI three-loop vertex resummed diagrams, then we are able to demonstrate that their leading (highly negative) powers cancel exactly. Also, for this form factor a smooth interpolation from extreme high-temperature suppression to unity at low temperatures suggests itself from the high-temperature behaviour already. In Sec. 6 we summarise our results and provide some outlook on future work.

## 2 Exclusion of sign configurations in massive bubble diagrams

In this section we count the number of energy-sign and scattering-channel combinations allowed by the constraints on momentum transfer in 4-vertices within 2PI diagrams that represent certain radiative corrections to the one-loop pressure,  $P|_{1\text{-loop}}$ , up to six loops. For the according Feynman rules in the massive sector, including these constraints, see [1]. By 2PI we understand those bubble diagrams that become 1-particle irreducible (1PI) contributions to the polarisation tensor upon cutting any single line.

A useful observation [18] concerning the momentum transfer constraints through 4-vertices is that the on-shellness of massive modes,  $p^2 = m^2 = 4e^2|\phi|^2$  ( $|\phi|$  being the modulus of the inert, adjoint scalar field associated with densely packed (anti)caloron centers in the thermal ground state [1, 13] setting the scale of maximal resolution) fixes the relative signs of the zero-components of four-momenta involved in the scattering process. For instance

$$|(p+q)^2| \leq |\phi|^2 \quad \Rightarrow \quad \text{sgn}(p_0) = -\text{sgn}(q_0), \quad (1)$$

$$|(p-q)^2| \leq |\phi|^2 \quad \Rightarrow \quad \text{sgn}(p_0) = \text{sgn}(q_0). \quad (2)$$

We here would like to investigate how these constraints decrease the number of sign configurations for loop momenta as the number of loops is increased in 2PI bubble diagrams contributing to the pressure. Subsequently, this general scheme is applied to 2PI bubble diagrams up to six loops: The ratio  $R$  of the allowed number of energy-sign and scattering-channel combinations to such a priori possible combination is computed for each diagram. We find that  $R$  decreases monotonically with increasing loop order but never vanishes. Indeed, we shall prove that within the class of dihedrally symmetric 2PI bubble diagrams  $R > 0$  at any finite loop order. The possibility to demonstrate termination of the loop expansion at a finite irreducible order [18] is therefore ruled out. Loosely speaking, this relates to the fact that the more symmetric bubble diagrams are the less independent their vertex constraints become. This very fact is ignored in the naive counting of the number of constraints per loop variable as performed in [22].

## 2.1 Exclusion tables

To analyse excluded sign configurations in a systematic way the following combinatorics applies: Let  $n$  be the number of vertices and  $N = 2n$  the number of internal lines. There are  $3^n$  a priori possible combinations of scattering channels (distinguished by invariant momentum transfer in the Mandelstam variables  $s, t$ , and  $u$ ) subject to their corresponding constraints. Moreover, there are  $2^N$  possible sign combinations for the zero-components in loop four-momenta. (The modulus of such a zero-component is bounded by mass  $m$ .) In analogy to [18] we organise all possible sign combinations in a table – one table for each vertex and scattering channel – and mark the excluded ones by gray elements. In this way, one obtains  $3n$  tables. The following table format is convenient. For  $N$  loop momenta, all zero-components can be positive ( $\binom{N}{0} = 1$  configurations, first row), only one zero-component is negative ( $\binom{N}{1} = N$  configurations, second row), two zero-components are negative ( $\binom{N}{2}$  configurations, third row), etc. Thus, there are  $N + 1$  rows in the table, the  $k$ -th row possessing  $\binom{N}{k-1}$  columns. For instance, setting  $n = 2$  there are four momenta  $a, b, c$ , and  $d$ . Thus, we assign the following a priori table:

$\emptyset$						
$a$	$b$	$c$	$d$			
$ab$	$ac$	$ad$	$bc$	$bd$	$cd$	
$a$	$b$	$c$	$d$			
$\emptyset$						

(3)

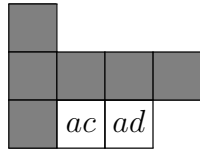
In the first row the symbol  $\emptyset$  denotes that  $a_0 > 0$  and  $b_0 > 0$  and  $c_0 > 0$ , and  $d_0 > 0$ , in the second row either  $a_0 < 0$  or  $b_0 < 0$  or  $c_0 < 0$ , or  $d_0 < 0$  and the others are positive, etc. Note that the constraints (1) and (2) determine relative signs only. Therefore, the exclusion tables are symmetric about the central row, and it is sufficient to consider the first  $N/2 + 1$  rows only. Moreover, the  $(N/2 + 1)$ th row is symmetric about its

center: The first entry is equivalent to the last, the second entry is equivalent to the second-to-last, and so forth. Therefore, the number of elements in the  $(N/2 + 1)$ th row can be halved. The overall-sign redundancy thus is completely removed by halving the number of elements in the table.

As an example, let us consider the  $s$ -channel constraint on the four-momenta  $a$ ,  $b$ ,  $c$ , and  $d$

$$|(a + b)^2| = |(c + d)^2| \leq |\phi|^2 \Rightarrow \text{sgn}(a_0) = -\text{sgn}(b_0), \text{sgn}(c_0) = -\text{sgn}(d_0). \quad (4)$$

At least two signs must differ from one another, ruling out row 1 and 2 (gray elements). In row 3 all combinations in which  $\text{sgn}(a_0) = \text{sgn}(b_0)$  or  $\text{sgn}(c_0) = \text{sgn}(d_0)$  are excluded. That is,  $a_0 > 0$  and  $b_0 > 0$  does not occur. This leaves only two options in total:



$$. \quad (5)$$

One proceeds by overlaying the tables for different vertices subject to given scattering channels. For a given element in the final table the overlay process enforces gray if at least one of the according elements in the contributing tables is gray. For example, a diagram with  $n = 3$  would or would not comprise the excluded combination  $s$ -channel on vertex 1,  $u$ -channel on vertex 2, and  $u$ -channel on vertex 3 ( $suu$ ) if an overlay of the exclusion tables for each associated vertex produced an entirely or partially gray table, respectively.

## 2.2 Exclusions for 2PI pressure diagrams up to six loops

For the radiative corrections due to the massive sector of deconfining  $SU(2)$  Yang-Mills thermodynamics bubble diagrams and their symmetry factors are identical to those of  $\lambda\varphi^4$ -theory [19]. Below we treat all 2PI diagrams up to six-loop order, and, due to limited space, we state explicit exclusion tables up to four loops only. For the computation of excluded sign combinations in five- and six-loop diagrams we resort to a Mathematica code whose notebook is available upon request from the authors. This code is also listed in [20]. It yields the ratio  $R$  of allowed vs.  $3^n \cdot 2^{2n-1}$  a priori possible (non-redundant) energy-sign and scattering-channel configurations<sup>2</sup>.

### 2.2.1 Two-loop diagram

The two-loop diagram in Figure 1 is subject to one vertex constraint only and was calculated in [16,21]. There is only one allowed sign-configuration:  $\text{sgn}(a_0) = -\text{sgn}(b_0)$  in this case. The modulus of the contribution from Figure 1 divided by the 1-loop result in the massive sector is less than  $3.5 \times 5 \cdot 10^{-6}$  everywhere in the deconfining phase.

<sup>2</sup>There are  $3^n$  channel combinations, each carrying  $2^{N-1} = 2^{2n-1}$  energy-sign combinations.

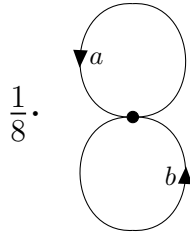


Figure 1: The only two-loop diagram (symmetry factor  $1/8$ ).

### 2.2.2 2PI three-loop diagram

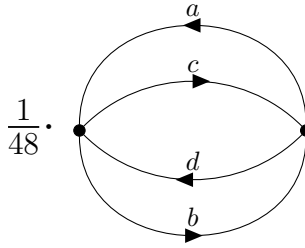


Figure 2: The only 2PI three-loop diagram (symmetry factor  $1/48$ ).

For the three-loop diagram in Figure 2 the a priori table is

$\emptyset$			
$a$	$b$	$c$	$d$
$ab$	$ac$	$ad$	

(6)

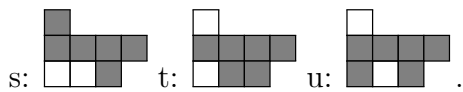
and both vertices are subject to the same set of  $s$ -,  $t$ -, and  $u$ -constraints. Namely,

$$s = |(a + d)^2| = |(b + c)^2| \leq |\phi|^2 \Rightarrow \text{sgn}(a_0) = -\text{sgn}(d_0), \text{sgn}(b_0) = -\text{sgn}(c_0) \quad (7)$$

$$t = |(a - b)^2| = |(c - d)^2| \leq |\phi|^2 \Rightarrow \text{sgn}(a_0) = \text{sgn}(b_0), \text{sgn}(c_0) = \text{sgn}(d_0) \quad (8)$$

$$u = |(a - c)^2| = |(d - b)^2| \leq |\phi|^2 \Rightarrow \text{sgn}(a_0) = \text{sgn}(c_0), \text{sgn}(d_0) = \text{sgn}(b_0). \quad (9)$$

This implies the following exclusion tables



By overlaying two such tables one infers that for  $ss$ ,  $tt$ , and  $uu$  there are two allowed sign configurations,

$$n(ss) = n(tt) = n(uu) = 2. \quad (10)$$

For  $st$ ,  $su$ , and  $tu$  only one allowed sign configuration remains,

$$n(st) = n(ts) = n(su) = n(us) = n(tu) = n(ut) = 1. \quad (11)$$

The numerator in the ratio  $R$  thus computes as

$$n(ss) + n(tt) + n(uu) + n(st) + n(ts) + n(su) + n(us) + n(tu) + n(ut) = 12. \quad (12)$$

Therefore, one obtains

$$R = 12/(9 \cdot 8) = 1/6 \quad (13)$$

for the diagram in [Figure 2](#).

### 2.2.3 2PI four-loop diagram

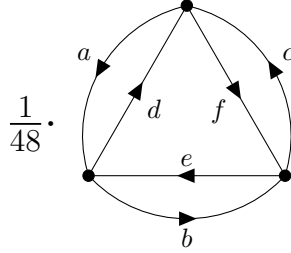


Figure 3: The only 2PI four-loop diagram (symmetry factor  $1/48$ ).

For the four-loop diagram in [Figure 3](#) we use the following channel conventions at each of the vertices  $V_1$ ,  $V_2$ , and  $V_3$

$V_1$ :

$$s = |(a + e)^2| = |(b + d)^2| \leq |\phi|^2 \Rightarrow \text{sgn}(a_0) = -\text{sgn}(b_0), \text{sgn}(c_0) = -\text{sgn}(d_0) \quad (14)$$

$$t = |(a - b)^2| = |(e - d)^2| \leq |\phi|^2 \Rightarrow \text{sgn}(a_0) = \text{sgn}(c_0), \text{sgn}(b_0) = \text{sgn}(d_0) \quad (15)$$

$$u = |(a - d)^2| = |(e - b)^2| \leq |\phi|^2 \Rightarrow \text{sgn}(a_0) = \text{sgn}(d_0), \text{sgn}(b_0) = \text{sgn}(c_0), \quad (16)$$

$V_2$ :

$$s = |(b + f)^2| = |(c + e)^2| \leq |\phi|^2 \Rightarrow \text{sgn}(e_0) = -\text{sgn}(b_0), \text{sgn}(f_0) = -\text{sgn}(d_0) \quad (17)$$

$$t = |(b - c)^2| = |(f - e)^2| \leq |\phi|^2 \Rightarrow \text{sgn}(f_0) = \text{sgn}(e_0), \text{sgn}(b_0) = \text{sgn}(d_0) \quad (18)$$

$$u = |(b - e)^2| = |(f - c)^2| \leq |\phi|^2 \Rightarrow \text{sgn}(e_0) = \text{sgn}(d_0), \text{sgn}(b_0) = \text{sgn}(f_0), \quad (19)$$

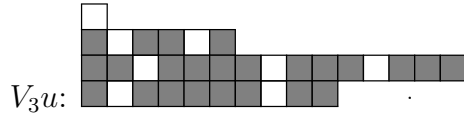
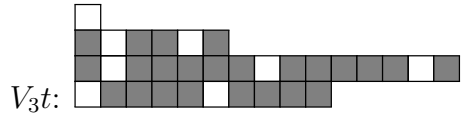
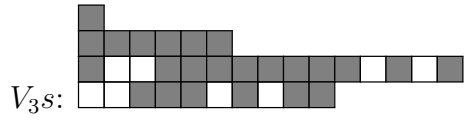
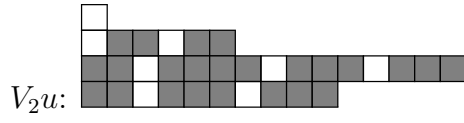
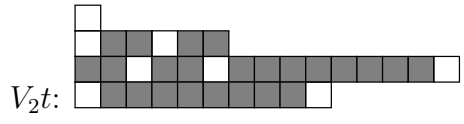
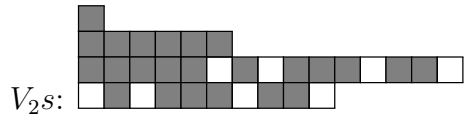
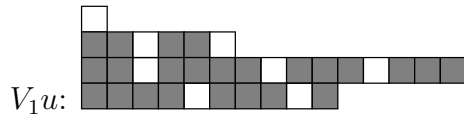
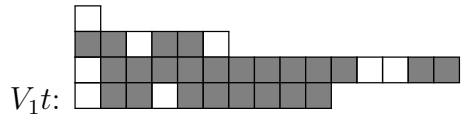
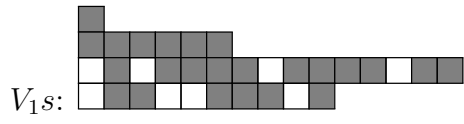
$V_3$ :

$$s = |(c + d)^2| = |(a + f)^2| \leq |\phi|^2 \Rightarrow \text{sgn}(c_0) = -\text{sgn}(e_0), \text{sgn}(f_0) = -\text{sgn}(a_0) \quad (20)$$

$$t = |(c - a)^2| = |(d - f)^2| \leq |\phi|^2 \Rightarrow \text{sgn}(a_0) = \text{sgn}(c_0), \text{sgn}(f_0) = \text{sgn}(e_0) \quad (21)$$

$$u = |(c - f)^2| = |(d - a)^2| \leq |\phi|^2 \Rightarrow \text{sgn}(c_0) = \text{sgn}(f_0), \text{sgn}(e_0) = \text{sgn}(a_0). \quad (22)$$





Channels	Allowed	Channels	Allowed	Channels	Allowed
$sss$	$abc$	$tss$	$cf, abc$	$uss$	$cf$
$sst$	$be, abc$	$tst$	$abc$	$ust$	$be$
$ssu$	$be$	$tsu$	$cf$	$usu$	$be, cf$
$sts$	$ad, abc$	$tts$	$abc$	$uts$	$ad$
$stt$	$abc$	$ttt$	$\emptyset, abc$	$utt$	$\emptyset$
$stu$	$ad$	$ttu$	$\emptyset$	$utu$	$\emptyset, ad$
$sus$	$ad$	$tus$	$cf$	$uus$	$ad, cf$
$sut$	$be$	$tut$	$\emptyset$	$uut$	$\emptyset, be$
$suu$	$ad, be$	$tuu$	$\emptyset, cf$	$uuu$	$\emptyset, ad, be, cf$

Table 1: Scattering channels and their respectively allowed sign configurations for the 2PI four-loop diagram in Figure 3. Sign configurations are denoted by their label in the 2PI four-loop a priori table (23). By  $\mathbb{Z}_2$ -symmetry (over-all sign flip), each label corresponds to *two* actual sign configurations. This means that, for instance,  $\emptyset$  denotes the configurations with all six zero components having the same sign,  $be$  denotes the configurations  $b^0, e^0 > 0 > a^0, c^0, d^0, f^0$  and  $b^0, e^0 < 0 < a^0, c^0, d^0, f^0$ , while  $abc$  denotes the configurations  $a^0, b^0, c^0 > 0 > d^0, e^0, f^0$  and  $a^0, b^0, c^0 < 0 < d^0, e^0, f^0$  and so forth (cf. Sec. 2.1) .

The allowed sign configurations for all 27 possible channel combinations are obtained by overlaying the respective tables and identifying the entries which are white thereafter. For example, the allowed sign configurations of the  $sss$ -channel are obtained by overlaying the tables  $V_1s$ ,  $V_2s$  and  $V_3s$ , where one finds that only the entry in the bottom left corner (with label  $abc$  in (23)) is white in all three tables. In Table 1 all channel combinations and their allowed energy-sign combinations, denoted by their label in the a priori table (23), are listed. Using this table, we conclude that

$$R = \frac{40}{864} = \frac{5}{108} = 0.0463. \quad (24)$$

#### 2.2.4 The two 2PI five-loop diagrams

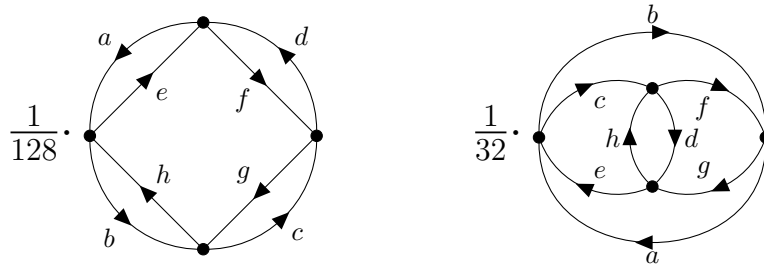


Figure 4: The first and second 2PI five-loop diagram (symmetry factors  $1/128$  (first) and  $1/32$  (second)).

The two 2PI five-loop diagrams are shown in [Figure 4](#). Instead of explicitly stating and comparing tables, which becomes increasingly tedious, we refer from here on to a Mathematica code to compute the ratio  $R$ . For the first and most symmetric diagram in [Figure 4](#) one obtains

$$R = 1/72 = 0.0139. \quad (25)$$

For the second diagram in [Figure 4](#) one computes

$$R = 1/81 = 0.0123. \quad (26)$$

### 2.2.5 The four 2PI six-loop diagrams

The four 2PI six-loop diagrams are shown in [Figure 5](#) and [Figure 6](#).

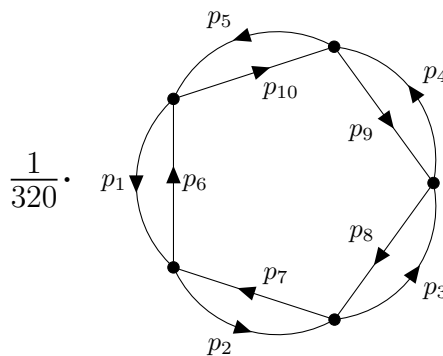


Figure 5: The first and most symmetric 2PI six-loop diagram (symmetry factor  $1/320$ ).

For the most symmetric diagram in [Figure 5](#) one obtains

$$R = 17/3888 = 0.0044, \quad (27)$$

for the other diagrams shown in [Figure 6](#), one has in the order of appearance

$$R = 7/1944 = 0.0036, \quad (28)$$

$$R = 13/3888 = 0.0033, \quad (29)$$

and

$$R = 1/324 = 0.0031. \quad (30)$$

### 2.2.6 Summary of results up to six loops

[Table 2](#) summarises our results for  $R$  and, as an aside, for the product  $R \cdot S$ ,  $S$  denoting the symmetry factor of a given diagram, up to 2PI six-loop order. Notice that while  $R$  drops with increasing loop order it is always finite. In fact, we prove in [Sec. 2.3](#) that there exists a class of 2PI diagrams (those with dihedral symmetry) for which  $R > 0$  at any finite loop order.

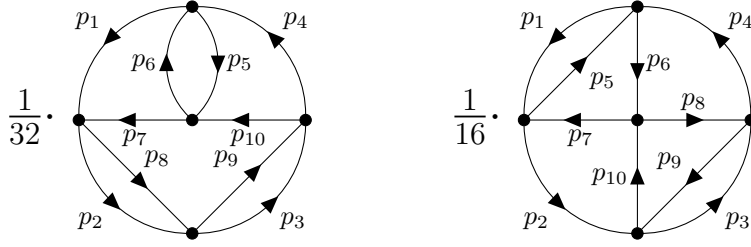


Figure 6a: The second and third 2PI six-loop diagrams (symmetry factors  $1/32$  and  $1/16$ ).

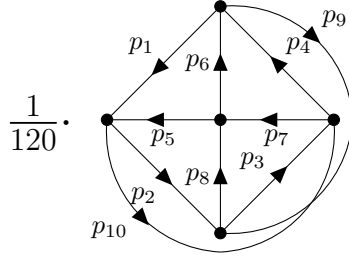


Figure 6b: The fourth 2PI six-loop diagram (symmetry factor  $1/120$ ). This is the only non-planar diagram up to six-loop order.

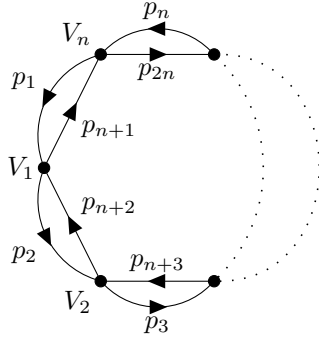
Loop number	Diagram number	$R$	$S^{-1}$	$R \cdot S$
3	1	0.1667	48	0.00347222
4	1	0.0463	48	0.00096451
5	1	0.0139	128	0.00010851
5	2	0.0123	32	0.00038580
6	1	0.0044	320	0.00001366
6	2	0.0036	32	0.00011253
6	3	0.0033	16	0.00020898
6	4	0.0033	120	0.00002572

Table 2: Ratio  $R$  of allowed vs. a priori possible energy-sign and scattering-channel combinations for 2PI bubble diagrams up to six loops.  $S$  denotes a diagram's symmetry factor.

### 2.3 Finiteness of $R$ at any finite loop order

Here we give a proof by induction showing that  $R > 0$  at any finite loop order within the class  $\mathcal{C}$  of diagrams symmetric under the dihedral group. That is, we address diagrams with the corners of an  $n$ -gon touching the enclosing circle. In other words, these diagrams represent a closed chain of pairs of momenta, tied together by  $n$  vertices. Examples are Figure 3 and the left diagram in Figure 4. Even though there is no such thing as a 2-gon, we admit the three-loop diagram in Figure 2 to this class.

We now prove that any diagram in class  $\mathcal{C}$  is subject to *one independent constraint only* provided that its vertices exclusively convey  $u$ -channel scattering. To set up the induction step, consider the case  $n \geq 3$ . We make the convention that momenta along the circle flow counter-clockwise and that momenta along the  $n$ -gon flow clockwise:



We define the  $u$ -channel momentum within a given vertex by subtracting the outgoing  $n$ -gon momentum from the ingoing circle momentum. According to this convention, the  $k$ -th vertex is  $u$ -channel constrained as

$$|(p_k - p_{n+k})^2| = |(p_{n+k+1} - p_{k+1})^2| \leq |\phi|^2, \quad (31)$$

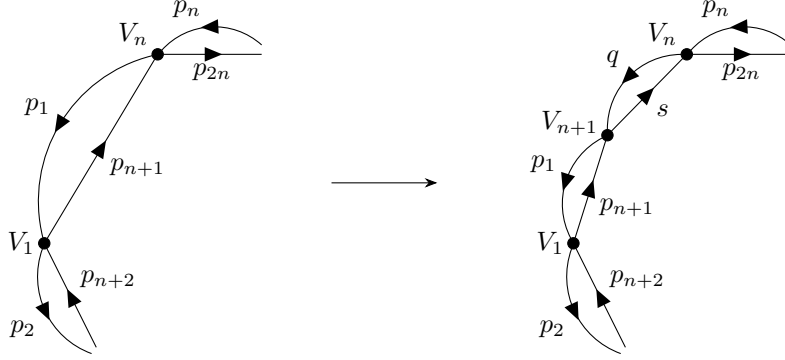
where  $k = 1, \dots, n-1$  and

$$|(p_n - p_{2n})^2| = |(p_{n+1} - p_1)^2| \leq |\phi|^2 \quad (32)$$

for  $k = n$ . These constraints are redundant by momentum conservation at each vertex. Namely,

$$\begin{aligned} |(p_1 - p_{n+1})^2| &= |(p_{n+2} - p_2)^2| = |(p_2 - p_{n+2})^2| = |(p_{n+3} - p_3)^2| = \dots = \\ &= |(p_n - p_{2n})^2| = |(p_{n+1} - p_1)^2| = |(p_1 - p_{n+1})^2| \leq |\phi|^2. \end{aligned} \quad (33)$$

To perform the induction step, we pinch in an extra vertex  $V_{n+1}$  inbetween  $V_n$  and  $V_1$ . This invokes new momenta  $q$  and  $s$  while  $p_1$  and  $p_{n+1}$  now link  $V_1$  and  $V_{n+1}$ .



Notice that the constraints on  $V_1$  up to  $V_{n-1}$  remain unchanged. On the other hand, the constraints on  $V_n$  and  $V_{n+1}$  read

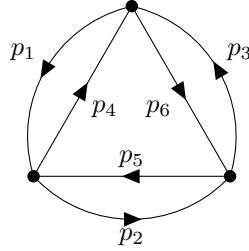
$$V_n : |(p_n - p_{2n})^2| = |(s - q)^2| \leq |\phi|^2 \quad (34)$$

$$V_{n+1} : |(q - s)^2| = |(p_{n+1} - p_1)^2| \leq |\phi|^2. \quad (35)$$

Thus, the chain in (33) can be continued up to  $V_{n+1}$ ,

$$\begin{aligned} |(p_1 - p_{n+1})^2| &= |(p_{n+2} - p_2)^2| = \dots = \\ &= |(p_n - p_{2n})^2| = |(s - q)^2| = |(p_{n+1} - p_1)^2| \leq |\phi|^2. \end{aligned} \quad (36)$$

Again, the extended chain is subject to *one independent constraint only*. It is obvious that the case  $n = 3$  (cf. Figure 3) shown below represents a valid induction base.



As a consequence, the support of the according loop integration is finite, independently of  $n$ . In turn, this implies  $R > 0$  for all diagrams within class  $\mathcal{C}$  which refutes the conjecture voiced in [22] that convergence of the 2PI loop expansion occurs by termination at a finite loop order. We are thus motivated to perform a more quantitative analysis of the diagrams in class  $\mathcal{C}$ , beginning at three-loop order. As we will demonstrate, the three-loop case splits into a contribution, which is subject to a single vertex constraint only, as well as a piece being subject to two independent constraints. The power of vertex constraints is impressively demonstrated by the a difference in leading power in  $\lambda$  of nine.

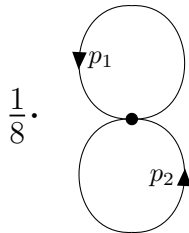


Figure 7: The two-loop diagram for the pressure in the massive sector of deconfining SU(2) Yang-Mills thermodynamics (symmetry factor 1/8).

### 3 Review of up to two-loop diagrams

As an interlude and to prepare the investigations performed in Secs. 4 and 5 we here review results on one-loop and two-loop diagrams within the massive sector of deconfining SU(2) Yang-Mills thermodynamics [16].

#### 3.1 One-loop pressure

On the level of free thermal quasiparticle excitations, that is, on the one-loop level the pressure exerted by the massive sector reads<sup>3</sup> [1]

$$P(\lambda)|_{1\text{-loop}} = -\Lambda^4 \frac{12\lambda^4}{(2\pi)^6} \bar{P}(2a), \quad (37)$$

where

$$\bar{P}(y) = \int_0^\infty dx x^2 \log \left[ 1 - e^{-\sqrt{x^2+y^2}} \right], \quad (38)$$

$\Lambda$  denotes the Yang-Mills scale,  $\lambda \equiv \frac{2\pi T}{\Lambda}$ , and  $a \equiv \frac{m}{2T}$ .

#### 3.2 Two-loop correction

The pressure contribution associated with the two-loop diagram in Figure 7 reads [16, 21]

$$\begin{aligned} \Delta P|_{2\text{-loop}} = & \frac{-2e^2 T^4}{\lambda^6} \int dr_1 dr_2 d\cos\theta \frac{r_1^2 r_2^2}{\sqrt{r_1^2 + m^2} \sqrt{r_2^2 + m^2}} \\ & \times \left[ 14 - 2 \frac{k^4}{m^4} \right] n_B \left( 2\pi \sqrt{\frac{r_1^2 + m^2}{\lambda^3}} \right) n_B \left( 2\pi \sqrt{\frac{r_2^2 + m^2}{\lambda^3}} \right), \quad (39) \end{aligned}$$

<sup>3</sup>We only quote that part of the pressure which is represented by excitations, the thermal ground state contributes a negative portion which is not considered here.

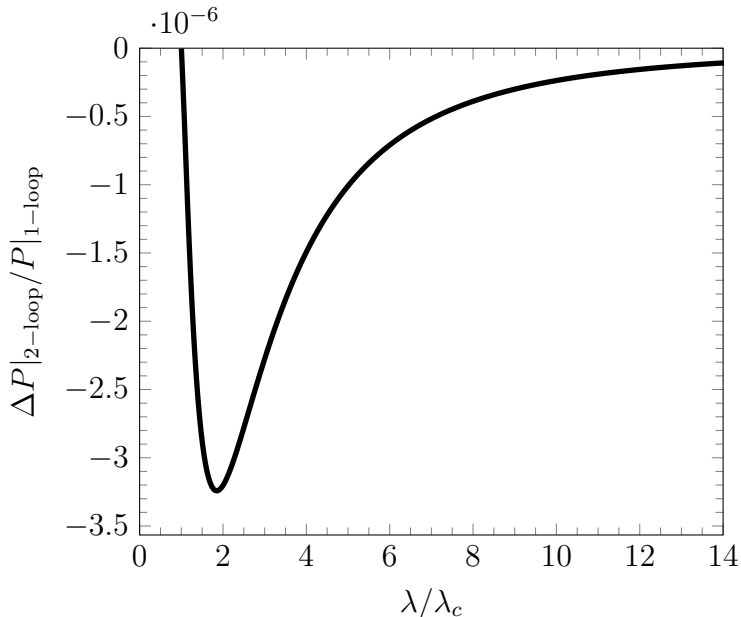


Figure 8: Plot of the ratio of two-loop vs. one-loop contributions to the pressure arising from the massive sector of deconfining SU(2) Yang-Mills thermodynamics as a function of dimensionless temperature  $\lambda = 2\pi\frac{T}{\Lambda}$ . The deconfining phase extends down to  $\lambda_c = 13.87$ .

where

$$k^2 \equiv p_1 p_2 = -\sqrt{r_1^2 + m^2} \sqrt{r_2^2 + m^2} - r_1 r_2 \cos \theta \quad (40)$$

is defined as the Lorentz-invariant product of the dimensionless<sup>4</sup> loop four-momenta  $p_1$  and  $p_2$ ,  $r_1 = |\mathbf{p}_1|$  and  $r_2 = |\mathbf{p}_2|$  denote the moduli of their spatial parts,  $n_B(x) = (\exp(x) - 1)^{-1}$  refers to the Bose-Einstein distribution function, and the integration is subject to the constraint

$$|2m^2 - 2\sqrt{r_1^2 + m^2} \sqrt{r_2^2 + m^2} - 2r_1 r_2 \cos \theta| \leq 1. \quad (41)$$

In Figure 8 the temperature dependence of the numerical integrations in (39) and (37) is shown in terms of their ratio.

## 4 The 2PI three-loop diagram

In the last section we have reviewed that the two-loop contribution to the pressure in the massive sector is strongly suppressed compared to the one-loop contribution for all temperatures. Because the results in [17] were based on an erroneous implementation of vertex constraints, a re-evaluation of the three-loop diagram in Figure 9 is required.

<sup>4</sup>We normalise physical four-momentum components  $P^\mu$  by  $|\phi|$  to arrive at dimensionless components  $p^\mu$ . Likewise, the physical mass is made dimensionless:  $m = 2e$ .

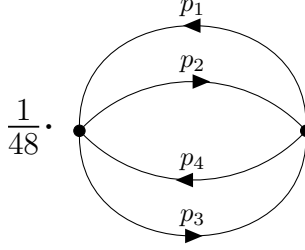


Figure 9: The 2PI three-loop diagram contributing to the pressure with symmetry factor  $1/48$

Interestingly, we find that a hierarchical suppression of three-loop vs. one-loop occurs only within a small band of low temperatures. As a consequence, the proper treatment of the radiative corrections induced by this particular diagram amounts to a resummation within an infinite class of higher loop diagrams. This resummation scheme will be addressed in Sec. 5 in terms of a particular truncation of the Dyson-Schwinger (DS) hierarchy. The resulting resummed chain is well bounded and hierarchically smaller than the one-loop contributions for *all* temperatures.

#### 4.1 Loop integral

Let us compute the diagram in Figure 9. To have an analytical grasp on it, we will perform a high-temperature expansion. Low temperatures are addressed by Monte Carlo methods. The consistency of both approaches is demonstrated by comparison within a transition regime.

To begin with, we quote the expression for the loop integral, derived in Appendix A, as

$$\Delta P|_{3\text{-loop}} = i \frac{\Lambda^4}{48\lambda^2} e^4 \frac{1}{(2\pi)^6} \sum_{\text{signs}} \int d\theta_1 d\varphi_1 dr_1 dr_2 d\theta_3 \sum_{\{r_3\}} r_1^2 r_2^2 r_3^2 \sin \theta_1 \sin \theta_3 \times P(p_i) \frac{n'_B(r_1) n'_B(r_2) n'_B(r_3) n'_B(r_4)}{8|p_1^0 p_2^0 p_3^0 p_4^0|}. \quad (42)$$

The first sum in (42) runs over allowed sign combinations for  $p_i^0$ ,  $i = 1, \dots, 4$ , see Appendix A. All four-momenta  $p_i \equiv (p_i^0, \mathbf{p}_i)$  are on-shell,  $|p_i^0| \equiv \sqrt{\mathbf{p}_i^2 + m^2}$ , and are parametrised as

$$p_4 \equiv p_2 + p_3 - p_1, \quad \mathbf{p}_2 \equiv \begin{pmatrix} 0 \\ 0 \\ r_2 \end{pmatrix}, \quad \mathbf{p}_3 \equiv r_3 \begin{pmatrix} 0 \\ \sin \theta_3 \\ \cos \theta_3 \end{pmatrix}, \quad \mathbf{p}_1 \equiv r_1 \begin{pmatrix} \sin \theta_1 \cos \varphi_1 \\ \sin \theta_1 \sin \varphi_1 \\ \cos \theta_1 \end{pmatrix}.$$

In the equivalent cases  $ss$ ,  $tt$ ,  $uu$  (diagonal), the integration is constrained by

$$|(p_1 + p_4)^2| = |(p_2 + p_3)|^2 \leq 1. \quad (43)$$

Summing over these cases, the resulting contribution to  $\Delta P|_{3\text{-loop}}$  is denoted by  $1/3\Delta P|_{3\text{-loop,ss}}$ . On the other hand, for the equivalent cases  $st, su, tu, ts, us, ut$  (off-diagonal) the constraints on the integration read

$$\begin{aligned} |(p_1 + p_4)^2| &= |(p_2 + p_3)|^2 \leq 1, \\ |(p_1 - p_2)^2| &= |(p_3 - p_4)|^2 \leq 1. \end{aligned} \quad (44)$$

The sum of these cases amounts to  $2/3\Delta P|_{3\text{-loop,st}}$  such that

$$\Delta P|_{3\text{-loop}} = \frac{1}{3}\Delta P|_{3\text{-loop,ss}} + \frac{2}{3}\Delta P|_{3\text{-loop,st}}. \quad (45)$$

The second sum in (42) runs over all solutions in  $r_3$  of the equation

$$\begin{aligned} \text{sgn}(p_2^0)\sqrt{r_2^2 + m^2} + \text{sgn}(p_3^0)\sqrt{r_3^2 + m^2} - \sqrt{r_1^2 + m^2} &= -[r_1^2 + r_2^2 + r_3^2 \\ -2r_1r_2 \cos \theta_1 - 2r_1r_3(\sin \varphi_1 \sin \theta_1 \sin \theta_3 + \cos \theta_1 \cos \theta_3) + 2r_2r_3 \cos \theta_3 + m^2]^{1/2}, \end{aligned} \quad (46)$$

see Appendix A. The polynomial  $P(\{p_i\})$  reads

$$\begin{aligned} P(\{p_i\}) &= 144 - 12\frac{1}{m^4} \left\{ (p_1p_2)^2 + (p_1p_3)^2 + (p_1p_4)^2 + (p_2p_3)^2 + (p_2p_4)^2 + (p_3p_4)^2 \right\} \\ &\quad + 36\frac{1}{m^6} \left\{ (p_1p_2)(p_1p_3)(p_2p_3) + (p_1p_2)(p_1p_4)(p_2p_4) \right. \\ &\quad \left. + (p_1p_3)(p_1p_4)(p_3p_4) + (p_2p_3)(p_2p_4)(p_3p_4) \right\} \\ &\quad + 12\frac{1}{m^8} \left\{ (p_1p_2)^2(p_3p_4)^2 + (p_1p_3)^2(p_2p_4)^2 + (p_1p_4)^2(p_2p_3)^2 - (p_1p_2)(p_1p_3)(p_2p_4)(p_3p_4) \right. \\ &\quad \left. - (p_1p_2)(p_1p_4)(p_2p_3)(p_3p_4) - (p_1p_3)(p_1p_4)(p_2p_3)(p_2p_4) \right\}, \end{aligned} \quad (47)$$

and the Bose-Einstein distribution shorthand notation is

$$n'_B(r) \equiv n_B \left( 2\pi\sqrt{r^2 + m^2}/\lambda^{3/2} \right). \quad (48)$$

In general, the constraints (43) and (44) cannot explicitly be resolved. Thus in a numerical evaluation of the integral one has to sample the regions that satisfy conditions (43), (44) and that solve (46), e.g. by the Monte Carlo method, while discarding complementary regions. However, as we demonstrate in Sec. 4.3, the high-temperature limit lends itself to an analytical resolution of (43), (44), and (46).

## 4.2 Properties of the vertex constraint

As a first step in understanding why  $\Delta P|_{3\text{-loop}}$  can be subjected to an analytical treatment at high temperatures it is necessary to elucidate the properties of the generic constraint (in dimensionless quantities)

$$|(a + b)^2| = |2m^2 - 2\sqrt{\mathbf{a}^2 + m^2}\sqrt{\mathbf{b}^2 + m^2} - 2|\mathbf{a}||\mathbf{b}|\cos \alpha| \leq 1, \quad (49)$$

where  $\alpha \equiv \angle \mathbf{a}\mathbf{b}$ . Recall from Sec. 2 that the plus sign in  $|(a+b)^2| \leq 1$  implies  $\text{sgn}(a^0) = -\text{sgn}(b^0)$ , explaining the sign in the second term on the right hand side. For later use, let us consider two limits. For small spatial momenta,  $|\mathbf{a}|, |\mathbf{b}| \ll 1$ , one has

$$|(a+b)^2| \approx |2m^2 - 2\sqrt{m^2}\sqrt{m^2}| = 0 < 1. \quad (50)$$

That is, angle  $\alpha$  becomes irrelevant. This can be made even more precise. It is straightforward to argue that

$$\begin{aligned} |(a+b)^2| &= |2m^2 - 2\sqrt{\mathbf{a}^2 + m^2}\sqrt{\mathbf{b}^2 + m^2} - 2|\mathbf{a}||\mathbf{b}|\cos\alpha| \\ &\leq |2m^2 - 2\sqrt{\mathbf{a}^2 + m^2}\sqrt{\mathbf{b}^2 + m^2} - 2|\mathbf{a}||\mathbf{b}||. \end{aligned} \quad (51)$$

For  $|\mathbf{a}| \leq 1/2$  and  $|\mathbf{b}| \leq 1/2$ , the right hand side of (51) can be estimated as

$$\begin{aligned} &|2m^2 - 2\sqrt{\mathbf{a}^2 + m^2}\sqrt{\mathbf{b}^2 + m^2} - 2|\mathbf{a}||\mathbf{b}|| \\ &\leq \left| 2m^2 - 2\left(\frac{1}{4} + m^2\right) - 2 \cdot \frac{1}{4} \right| = \left| -\frac{1}{2} - \frac{1}{2} \right| = 1. \end{aligned} \quad (52)$$

As a consequence, (49) is satisfied independently of angle  $\alpha$  if  $|\mathbf{a}| \leq 1/2$  and  $|\mathbf{b}| \leq 1/2$ . However, this region yields a small contribution to  $\Delta P|_{3\text{-loop}}$ , in particular at high temperatures.

The second (and much more relevant) limit  $|\mathbf{a}|, |\mathbf{b}| \gg 1$  requires  $\alpha$  to be close to  $\pi$  and  $|a| \approx |b|$ . This is demonstrated by rendering the constraint (49) an equation by letting the right hand side vary as

$$(a+b)^2 = -z, \quad z \in [-1, 1]. \quad (53)$$

Solving (53) for  $\cos\alpha$  yields

$$\cos\alpha = \frac{z + 2m^2 - 2\sqrt{\mathbf{a}^2 + m^2}\sqrt{\mathbf{b}^2 + m^2}}{2|\mathbf{a}||\mathbf{b}|}. \quad (54)$$

For  $|\mathbf{a}|, |\mathbf{b}| \gg m$  the condition  $\cos\alpha \geq -1$  implies  $z \geq 0$ , i.e.  $z \in [0, 1]$ . Moreover,  $\cos\alpha$  is maximised for fixed  $|\mathbf{a}|$  and  $z$  by

$$|\mathbf{b}| = |\mathbf{a}|m\sqrt{\frac{4m^2 - \frac{4m^2z}{|\mathbf{a}|^2} - \frac{z^2}{|\mathbf{a}|^2}}{4m^4 + 4m^2z + z^2}}, \quad (55)$$

yielding, to leading order in  $1/|\mathbf{a}|$ ,

$$\cos\alpha \approx -1 + \frac{1}{2|\mathbf{a}|^2} \left( z + \frac{z^2}{4m^2} \right). \quad (56)$$

Hence,  $\cos\alpha$  is maximised by  $z = 1$  at fixed  $|\mathbf{a}|$ . The numerical value of the factor  $1 + 1/(4m^2)$  is approximately 1.00079 at high temperatures ( $m = 2e = 2\sqrt{8\pi}$ ). This

amounts to the width  $\Delta\alpha$  of the band of allowed angles becoming narrower as  $|\mathbf{a}| \rightarrow \infty$  like

$$\Delta\alpha = \pi - \arccos\left(-1 + \frac{1}{2|\mathbf{a}|^2} \left(1 + \frac{1}{4m^2}\right)\right) \approx \frac{1}{|\mathbf{a}|} \sqrt{1 + \frac{1}{4m^2}} \quad (57)$$

to leading order in  $1/|\mathbf{a}|$ . Similarly, we derive the width  $\Delta|\mathbf{b}|$  of the band of allowed values of  $|\mathbf{b}|$  as follows: One can solve (53) for  $|\mathbf{b}|$ , which is a quadratic equation and thus yields two values for  $|\mathbf{b}|$ . Their difference is maximised at  $\cos\alpha = -1$ . These two solutions at  $\cos\alpha = -1$ , referred to as  $|\mathbf{b}|_{\max/\min}$ , are given by

$$|\mathbf{b}|_{\max/\min} = |\mathbf{a}| \left(1 + \frac{z}{2m^2} \pm \frac{1}{2} \sqrt{4\frac{z}{m^2} + \frac{z^2}{m^4} + \frac{4z}{|\mathbf{a}|^2} + \frac{z^2}{|\mathbf{a}|^2 m^2}}\right). \quad (58)$$

Again, their difference is maximised by  $z = 1$ , and variation of parameter  $z \in [0, 1]$  implies that all  $|\mathbf{b}|$  between  $|\mathbf{b}|_{\max, z=1}$  and  $|\mathbf{b}|_{\min, z=1}$  are consistent with the constraint (49). At large  $|\mathbf{a}|$  (58) approaches

$$|\mathbf{b}|_{\max/\min, z=1} = |\mathbf{a}| \left(1 + \frac{1}{2m^2} \pm \frac{1}{2} \sqrt{\frac{4}{m^2} + \frac{1}{m^4}}\right) \approx |\mathbf{a}| (1.002 \pm 0.056) \quad (59)$$

where the expression to the far right, again, is obtained for the high-temperature value of  $m$ :  $m = 2\sqrt{8}\pi$ . This means that allowed band of  $|\mathbf{b}|$  values broadens in the limit  $|\mathbf{a}| \rightarrow \infty$  and has a width of approximately 11% of  $|\mathbf{a}|$ . The above limits for  $\Delta\alpha$  and  $|\mathbf{b}|_{\max/\min}$  are rapidly approached, see Figure 10.

### 4.3 High-temperature analysis

Returning to the 3-loop integral (42), we aim for an approximation in the high-temperature situation  $\lambda \gg \lambda_c$ . Then the only temperature dependent entities within the integrand are the Bose factors since mass and coupling saturate to  $m = 2e = 2\sqrt{8}\pi$ . Let us exhibit why the limit  $r_1, r_2 \gg m$  is relevant. The variables  $r_1$  and  $r_2$  are integrated up to infinity but the factors of

$$n_B \left(2\pi \sqrt{r_{1,2}^2 + m^2} / \lambda^{3/2}\right) \quad (60)$$

start to suppress the integrand when  $2\pi(r_{1,2}^2 + m^2)^{1/2} \gtrsim \lambda^{3/2} \log(2)$ . The other factors in the integrand of (42) amount to a polynomial in radial (and other) variables, when considering this regime at high temperatures to approximate  $(r_{1,2}^2 + m^2)^{1/2} \approx r_{1,2}$ . Hence, we expect terms proportional to  $r_{1,2}^M n'_B(r_{1,2})$  to be integrated over, where  $M \leq N$  and  $N$  is the (yet unknown) order of the polynomial. Since we are considering the limit of large  $r_{1,2}$  the highest order term  $r_{1,2}^N n'_B(r_{1,2})$  should dominate. Regardless of the exact power  $N$  (as long as it is greater than one), one obtains a curve similar to the Planck law, as shown in Figure 11 for several powers. The position of the maximum  $r_{1,2;\max}$  is in all cases proportional to  $\lambda^{3/2}$ , and hence the integration is expected to be dominated

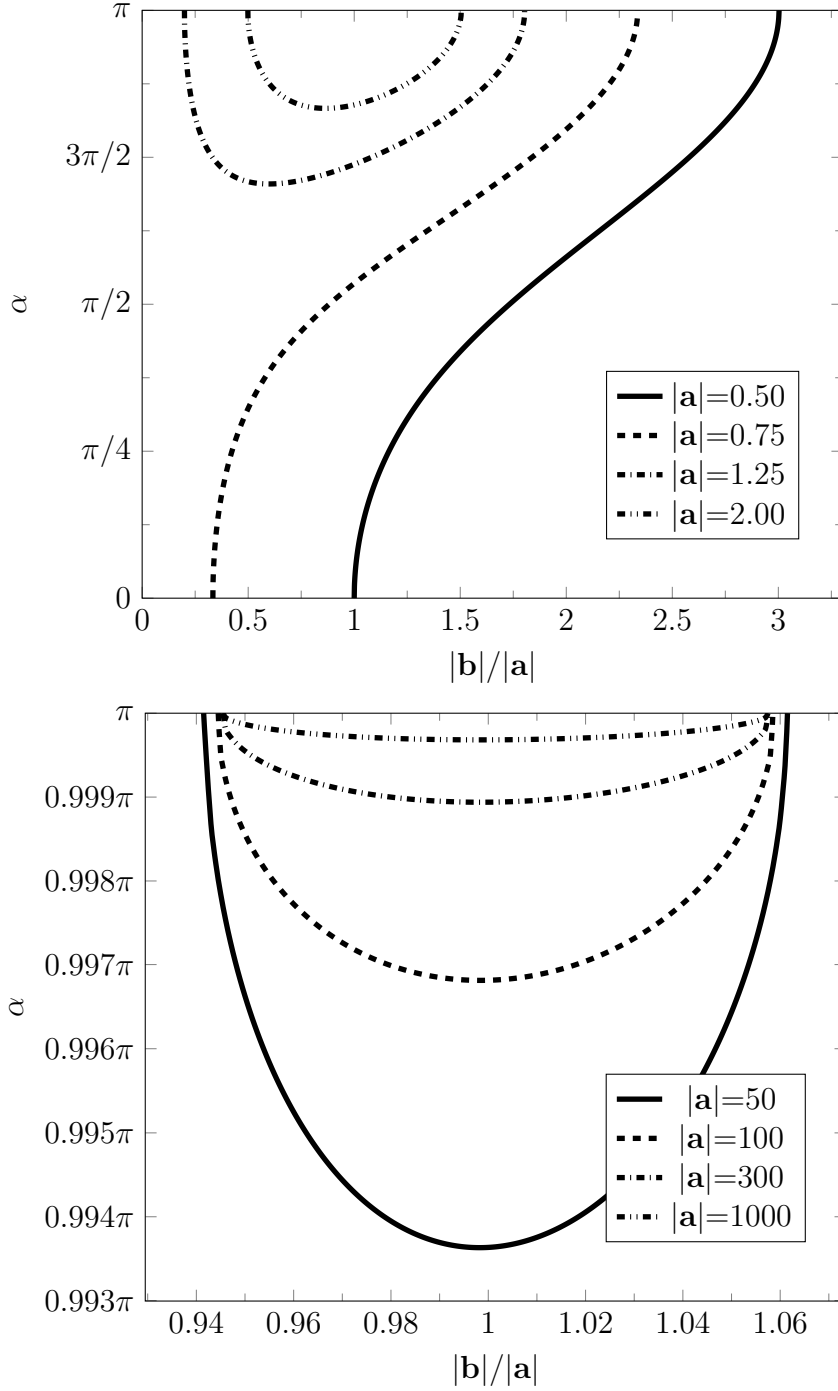


Figure 10: Visualisation of  $\alpha = \langle \mathbf{a}\mathbf{b} \rangle$  as a function of  $|\mathbf{b}|/|\mathbf{a}|$  for small and large values of  $|\mathbf{a}|$ , obtained by saturating the constraint to  $(a + b)^2 = -1$  and setting the mass equal to the plateau value  $m = 2\sqrt{8}\pi$ . The interpretation is that only coordinates above the lines are admitted by the constraint. When  $|\mathbf{a}|$  surpasses 1, one approaches the situation described by (57) and (59), namely the width  $\Delta\alpha$  approaches  $|\mathbf{a}|^{-1}$  and the width  $\Delta|\mathbf{b}|/|\mathbf{a}|$  approaches 0.113 as  $|\mathbf{a}| \rightarrow \infty$ .

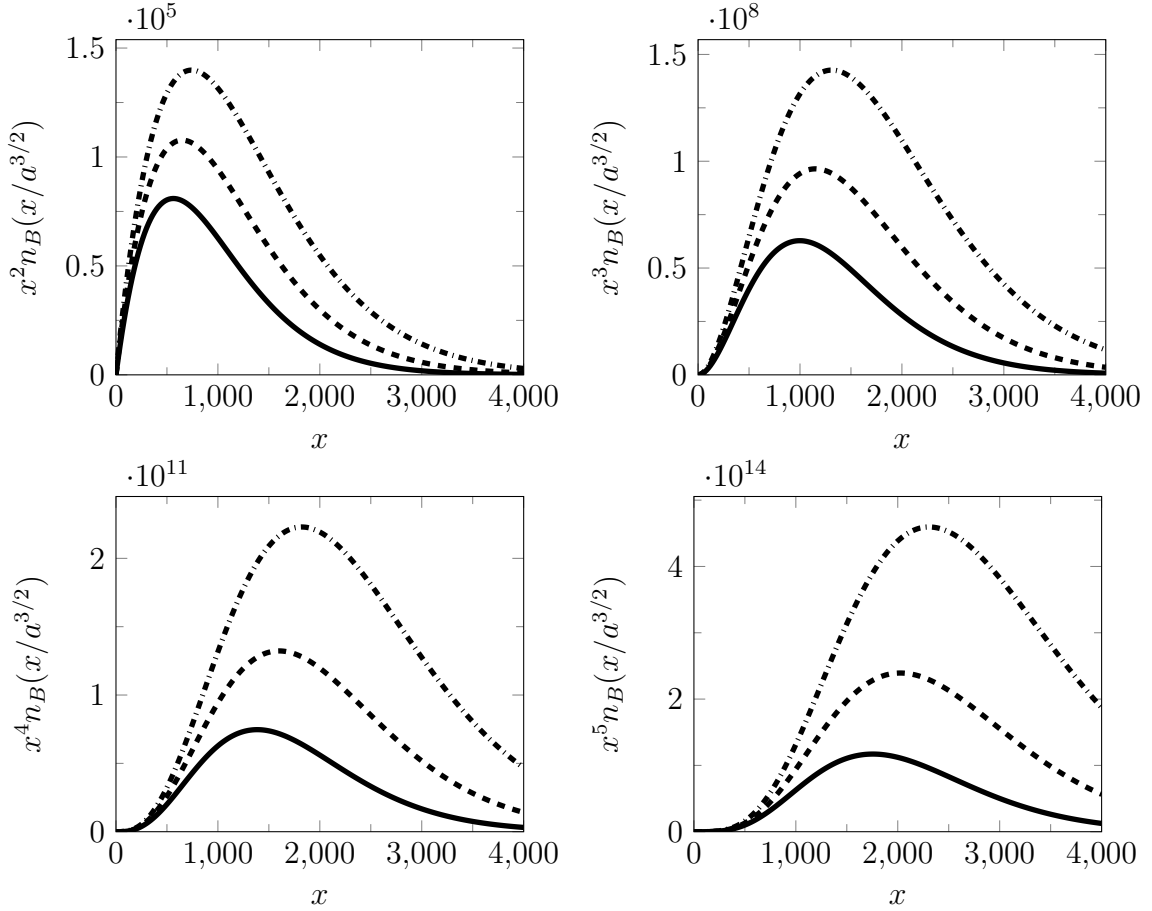


Figure 11: Plot of  $f(x) = x^N n_B(x/a^{3/2})$ , for  $N = 2, 3, 4, 5$  and  $a = 50$  (solid lines),  $a = 55$  (dashed lines),  $a = 60$  (dashdotted lines). This demonstrates that the qualitative features do not depend on  $N \geq 2$ . At fixed  $N$ , maxima are shifted towards larger  $x$  and  $f(x)$  as  $a$  increases. At fixed  $a$ , increasing  $N$  also shifts the position of the maxima to larger  $x$  and  $f(x)$  increases by several orders of magnitude.

by a small region centered at this maximum. This justifies to consider  $r_1, r_2 \gg m$ . The diagonal contribution indeed is self-consistently given by this limit and subject to considerable simplifications.

From the discussion in Sec. 4.2 we know that for the  $s$ -channel constraint  $|(p_1^2 + p_4^2)| = |(p_2^2 + p_3^2)| \leq 1$  one has  $\cos \angle \mathbf{p}_1 \mathbf{p}_4 \approx -1$  and  $\cos \angle \mathbf{p}_2 \mathbf{p}_3 \approx -1$  and, using  $\cos(\pi - \alpha) = -\cos \alpha$ , we conclude

$$\cos \angle \mathbf{p}_1 \mathbf{p}_2 = \cos \theta_1 \approx -\cos \angle \mathbf{p}_1 \mathbf{p}_3 \approx -\cos \angle \mathbf{p}_2 \mathbf{p}_4 \approx \cos \angle \mathbf{p}_3 \mathbf{p}_4. \quad (61)$$

Exploiting these relations, (46) simplifies to

$$\begin{aligned} \text{sgn}(p_2^0) \sqrt{r_2^2 + m^2} + \text{sgn}(p_3^0) \sqrt{r_3^2 + m^2} - \sqrt{r_1^2 + m^2} = & -[r_1^2 + r_2^2 + r_3^2 \\ & - 2r_1 r_2 \cos \theta_1 + 2r_1 r_3 \cos \theta_1 - 2r_2 r_3 + m^2]^{1/2}. \end{aligned} \quad (62)$$

Recalling that  $\text{sgn}(p_2^0) = -\text{sgn}(p_3^0)$  for all allowed sign configurations in the first sum of (42), this is solved by  $r_3 = r_2$ . Assuming  $r_1, r_2 > 50$  and  $r_3 > 0$ , Mathematica confirms that this solution is unique. Thus it is legitimate in this limit to execute the sum over  $r_3$  simply by replacing  $r_3$  by  $r_2$ . Conveniently, this also implies  $r_4 = r_1$  which, in turn, entails that  $p_1^0 = -p_4^0$  and  $p_2^0 = -p_3^0$ . Thus the two scalar products of four vectors reduce to

$$p_1 p_4 = p_1^0 p_4^0 - r_1 r_4 \cos \angle \mathbf{p}_1 \mathbf{p}_4 \approx -(p_1^0)^2 + r_1^2 = -m^2 \quad (63)$$

$$p_2 p_3 = p_2^0 p_3^0 - r_2 r_4 \cos \angle \mathbf{p}_2 \mathbf{p}_3 \approx -(p_2^0)^2 + r_2^2 = -m^2, \quad (64)$$

and the remaining ones are expressed in terms of  $p_1 p_2$  as

$$p_1 p_2 = p_1^0 p_2^0 - r_1 r_2 \cos \angle \mathbf{p}_1 \mathbf{p}_2 \quad (65)$$

$$p_1 p_3 \approx -p_1^0 p_2^0 + r_1 r_2 \cos \angle \mathbf{p}_1 \mathbf{p}_2 = -p_1 p_2 \quad (66)$$

$$p_2 p_4 \approx -p_1^0 p_2^0 + r_1 r_2 \cos \angle \mathbf{p}_1 \mathbf{p}_2 = -p_1 p_2 \quad (67)$$

$$p_3 p_4 \approx p_1^0 p_2^0 - r_1 r_2 \cos \angle \mathbf{p}_1 \mathbf{p}_2 = p_1 p_2. \quad (68)$$

$$(69)$$

Therefore, the only independent invariants in the polynomial in (47) are  $m$  and

$$k^2(r_1, r_2, \theta_1) \equiv |p_1 p_2|, \quad (70)$$

and one can recast  $P(\{p_i\})$  as

$$\begin{aligned} & 144 - 12 \frac{1}{m^4} [2m^4 + 4k^4] + 36 \frac{1}{m^6} [4m^2 k^4] + 12 \frac{1}{m^8} [k^8 + m^8 - 2k^4 m^4] \\ & = 132 + 72 \frac{k^4}{m^4} + 12 \frac{k^8}{m^8} \end{aligned} \quad (71)$$

which is strictly positive. The integrand of (42) reduces to

$$r_1^2 r_2^4 \sin \theta_1 \sin \theta_3 \left( 132 + 72 \frac{k^4}{m^4} + 12 \frac{k^8}{m^8} \right) \frac{n_B'^2(r_1) n_B'^2(r_2)}{8(r_1^2 + m^2)(r_2^2 + m^2)}, \quad (72)$$

which, besides the factor  $\sin \theta_3$ , merely depends on  $r_1, r_2$ , and  $\theta_1$ . The  $\phi_1$ -integration can be executed trivially to yield a factor of  $2\pi$ . The factor of  $\sin \theta_3$  appears to enforce the vanishing of the entire integral at first sight since we have assumed  $\theta_3 = \pi$ . However, we know from the discussion in Sec. 4.2 that the width of the allowed deviation of  $\theta_3$  from  $\pi$  is given by

$$\Delta \theta_3 = \pi - \arccos \left( -1 + \frac{1}{2r_2^2} \left( 1 + \frac{1}{4m^2} \right) \right) \approx \frac{1}{r_2} \sqrt{1 + \frac{1}{4m^2}}. \quad (73)$$

Since this is increasingly small, the integration can be approximated by applying a mean value  $\bar{\theta}_3 = \pi - \Delta \theta_3 / 2$  as a function of  $r_2$  and by multiplying this with the width  $\Delta \theta_3$ :

$$\int_0^\pi d\theta_3 \longrightarrow \int_0^\pi d\theta_3 \delta(\theta_3 - \bar{\theta}_3) \Delta \theta_3. \quad (74)$$

The full integral, subject to the remaining integrations over  $r_1$ ,  $r_2$ , and  $\theta_1$ , thus reads

$$i \frac{\Lambda^4}{48\lambda^2} e^4 \frac{1}{(2\pi)^5} \sum_{\text{signs}} \int d\theta_1 dr_1 dr_2 r_1^2 r_2^4 \sin \theta_1 \sin(\Delta\theta_3/2) \Delta\theta_3 \\ \times \left( 132 + 72 \frac{k^4}{m^4} + 12 \frac{k^8}{m^8} \right) \frac{n_B'^2(r_1) n_B'^2(r_2)}{8(r_1^2 + m^2)(r_2^2 + m^2)} \quad (75)$$

where we have used that  $\sin(\pi - x) = \sin(x)$ . We now specialise to the diagonal contribution. (In the off-diagonal case the integration is further constrained by  $|(p_1 - p_2)^2| \leq 1$ .)

In the diagonal case, the integration over  $\theta_1$  is unconstrained and thus for the first term of the residual polynomial (71) the  $\theta_1$ -integral over  $\text{const.} \times \sin \theta_1$  amounts to a factor of 2. For the second and third term consider that

$$\int_0^\pi d\theta \sin \theta \cos^n \theta \quad (76)$$

vanishes for odd  $n$ . Therefore, all sign dependence in  $k^4$  and  $k^8$  drops out after integrating over  $\theta_1$ ,

$$k^4 = (r_1^2 + m^2)(r_2^2 + m^2) + r_1^2 r_2^2 \cos^2 \theta_1 \pm 2\sqrt{(r_1^2 + m^2)(r_2^2 + m^2)} r_1 r_2 \cos \theta_1, \\ = m^4 + m^2(r_1^2 + r_2^2) + r_1^2 r_2^2 (1 + \cos^2 \theta_1) \\ \pm 2\sqrt{(r_1^2 + m^2)(r_2^2 + m^2)} r_1 r_2 \cos \theta_1 \quad (77)$$

$$k^8 = m^8 + (r_1^2 + r_2^2)2m^6 + r_1^2 r_2^2 m^4 (4 + 6 \cos^2 \theta_1) + (r_1^4 + r_2^4) m^4 \\ (r_1^4 r_2^2 m^2 + r_1^2 r_2^4 m^2) \cdot (2 + 6 \cos^2 \theta_1) + r_1^4 r_2^4 (1 + 6 \cos^2 \theta_1 + \cos^4 \theta_1) \\ \pm [\propto \cos^{(\text{odd})}].$$

Hence  $\theta_1$  can explicitly be integrated away, and, since the sign dependence is lost, the sum over signs simply amounts to a factor given by the number of possible energy-sign combinations. This factor is two in the diagonal case, see Sec. 2.2.2. Upon processing all numerical factors in (75) further, we arrive at

$$\frac{1}{3} \Delta P|_{3\text{-loop,ss}} = i \frac{\Lambda^4}{\lambda^2} e^4 \frac{1}{(2\pi)^5} \int dr_1 dr_2 \frac{r_1^2 r_2^4}{(r_1^2 + m^2)(r_2^2 + m^2)} \sin(\Delta\theta_3/2) \Delta\theta_3 \\ \times \left( \frac{3}{4} + \frac{1}{3} \frac{r_1^2 + r_2^2}{m^2} + \frac{7}{12} \frac{r_1^2 r_2^2}{m^4} + \frac{1}{24} \frac{r_1^4 + r_2^4}{m^4} + \frac{1}{6} \frac{r_1^4 r_2^2 + r_1^2 r_2^4}{m^6} + \frac{2}{15} \frac{r_1^4 r_2^4}{m^8} \right) \\ \times n_B'^2(r_1) n_B'^2(r_2), \quad (78)$$

and we finally explicitly observe the anticipated polynomial structure in  $r_1$  and  $r_2$ . Our assumption that the integrand is dominated by large  $r_1$  and  $r_2$  hence turns out to be self-consistent. Equation (78) represents the high-temperature limit of (42), and

the remaining integrals can be performed numerically. Before we treat the off-diagonal case, we demonstrate how the leading power in  $\lambda$  can be extracted in (78). Using

$$\Delta\theta \approx \frac{1}{r_2} \sqrt{1 + \frac{1}{4m^2}} \quad \sin(\Delta\theta_3/2) \approx \frac{1}{2r_2} \sqrt{1 + \frac{1}{4m^2}} \quad (79)$$

simplifies (78) as

$$\begin{aligned} \frac{1}{3} \Delta P|_{3\text{-loop,ss}} &= i \frac{\Lambda^4}{\lambda^2} e^4 \frac{1}{(2\pi)^5} \left(1 + \frac{1}{4m^2}\right) 4m^2 \int dr_1 dr_2 \frac{r_1^2 r_2^2}{(r_1^2 + m^2)(r_2^2 + m^2)} \\ &\times \left( \frac{3}{8} + \frac{1}{6} \frac{r_1^2 + r_2^2}{m^2} + \frac{7}{24} \frac{r_1^2 r_2^2}{m^4} + \frac{1}{48} \frac{r_1^4 + r_2^4}{m^4} + \frac{1}{12} \frac{r_1^4 r_2^2 + r_1^2 r_2^4}{m^6} + \frac{1}{15} \frac{r_1^4 r_2^4}{m^8} \right) \\ &\times n_B^{\prime 2}(p_1) n_B^{\prime 2}(p_2). \quad (80) \end{aligned}$$

Since the integrations over  $r_1$  and  $r_2$  in (80) are independent from one another some factorisation subject to the following factors occurs

$$\begin{aligned} I_1 &= \int dx \frac{x^2}{x^2 + m^2} n_B^2 \left( 2\pi \sqrt{\frac{x^2 + m^2}{\lambda^3}} \right), \\ I_2 &= \int dx \frac{x^4}{x^2 + m^2} n_B^2 \left( 2\pi \sqrt{\frac{x^2 + m^2}{\lambda^3}} \right), \\ I_3 &= \int dx \frac{x^6}{x^2 + m^2} n_B^2 \left( 2\pi \sqrt{\frac{x^2 + m^2}{\lambda^3}} \right). \end{aligned} \quad (81)$$

Although only  $I_3$  turns out to be relevant for the leading order in  $\lambda$  let us analyse all three integrals in a high-temperature situation. Namely, for sufficiently large  $\lambda$  one can split  $I_1$  into a first part  $I_1^{\hat{x}}$ , integrated up to an arbitrary parameter  $\hat{x}$  such that  $m \ll \hat{x} \ll \lambda^{3/2} \log(2)/(2\pi)$  and a second part  $I_1^\infty$  from  $\hat{x}$  to infinity. For simplicity, we choose  $\hat{x} = \lambda$ . For the integration in  $I_1^{\hat{x}}$  we may apply

$$n_B \left( 2\pi \sqrt{\frac{x^2 + m^2}{\lambda^3}} \right) \approx \frac{1}{1 + 2\pi \sqrt{\frac{x^2 + m^2}{\lambda^3}} - 1} = \frac{1}{2\pi} \sqrt{\frac{\lambda^3}{(x^2 + m^2)}}. \quad (82)$$

Therefore,  $I_1^{\hat{x}}$  can be approximated as

$$\begin{aligned} I_1^{\hat{x}} &\approx \frac{\lambda^3}{4\pi^2} \int_0^{\hat{x}} dx \frac{x^2}{(x^2 + m^2)^2} = \frac{\lambda^3}{4\pi^2 m} \int_0^{\hat{y}} dy \frac{y^2}{(y^2 + 1)^2} \\ &= \frac{\lambda^3}{4\pi^2 m} \frac{1}{2} \left( \left[ -\frac{y}{y^2 + 1} \right]_0^{\hat{y}} + \int_0^{\hat{y}} dy \frac{1}{y^2 + 1} \right) \\ &= \frac{\lambda^3}{8\pi^2} \left( -\frac{\hat{x}}{\hat{x}^2 + m^2} + \frac{\arctan\left(\frac{\hat{x}}{m}\right)}{m} \right), \\ &\approx \frac{\lambda^3}{16\pi m} - \frac{\lambda^2}{8\pi^2}, \end{aligned} \quad (83)$$

where  $y \equiv x/m$ , and  $\arctan\left(\frac{\hat{x}}{m}\right) \approx \pi/2$ . For the remaining integral  $I_1^\infty$  the prefactor of  $n_B^2$  in the integrand is close to unity, and we obtain

$$\begin{aligned} I_1^\infty &\approx \int_{\hat{x}}^\infty dx n_B^2 \left( 2\pi \sqrt{\frac{x^2 + m^2}{\lambda^3}} \right) = \frac{\lambda^{3/2}}{2\pi} \int_{\hat{y}}^\infty dy n_B^2(y) \\ &= \frac{\lambda^{3/2}}{2\pi} [-\hat{y} + n_B(\hat{y}) + \log(e^{\hat{y}} - 1)] \\ &\approx -\lambda + \frac{\lambda^2}{4\pi^2} - \frac{\lambda^{3/2}}{2\pi} \log\left(\frac{\lambda^{1/2}}{2\pi}\right), \end{aligned} \quad (84)$$

where  $y \equiv 2\pi x/\lambda^{3/2}$ . Thus, indeed, the contribution of leading power three in  $\lambda$  resides in  $I_1^\infty$ , and we conclude

$$I_1 \approx \frac{\lambda^3}{16\pi m} \quad (85)$$

for sufficiently high  $\lambda$ .  $I_2$  and  $I_3$  are, due to the higher powers in the prefactors of  $n_B^2$  in the respective integrands, strongly dominated by  $x^2 \gg m^2$  and thus we can approximate

$$I_2 \approx \int_0^\infty dx x^2 n_B^2 \left( 2\pi \sqrt{\frac{x^2}{\lambda^3}} \right) = \frac{\lambda^{9/2}}{(2\pi)^3} \int_0^\infty dy y^2 n_B^2(y) = \frac{\lambda^{9/2}}{(2\pi)^3 \cdot 3} (\pi^2 - 6\zeta(3))$$

and

$$I_3 \approx \int_0^\infty dx x^4 n_B^2 \left( 2\pi \sqrt{\frac{x^2}{\lambda^3}} \right) = \frac{\lambda^{15/2}}{(2\pi)^5} \int_0^\infty dy y^4 n_B^2(y) = \frac{\lambda^{15/2}}{(2\pi)^5} \frac{4}{15} (\pi^4 - 90\zeta(5))$$

where  $\zeta(z)$  denotes Riemann's zeta function, and we have substituted  $y = 2\pi x/\lambda^{3/2}$ . Thus, to leading order in  $\lambda$  we have

$$\begin{aligned} \frac{1}{3} \Delta P|_{3\text{-loop,ss}} &= i \frac{\Lambda^4}{\lambda^2} e^4 \frac{1}{(2\pi)^5} \frac{1}{15} \left( 1 + \frac{1}{4m^2} \right) \frac{I_3^2}{m^8} \\ &= i \Lambda^4 \frac{1}{3375} \frac{1}{(2\pi)^{15}} \frac{1}{m^4} \left( 1 + \frac{1}{4m^2} \right) (\pi^4 - 90\zeta(5))^2 \lambda^{13} \\ &\equiv i c_{13} \Lambda^4 \lambda^{13} \end{aligned} \quad (86)$$

for  $\lambda \gg \lambda_c$ . In (86)  $m = 2e$  was used. The numerical value of coefficient  $c_{13}$  is

$$c_{13} = 5.2968 \cdot 10^{-20}. \quad (87)$$

This value is confirmed by a fit to the numerical integration of (78).

Returning to the off-diagonal case, one has to assert  $|(p_1 - p_2)^2| \leq 1$  in (75). In this case the limit  $r_1, r_2 \gg 1$  implies that  $\theta_1 \approx 0$  instead of  $\pi$ , and one can estimate

the width and mean value of the allowed band for  $\theta_1$  in the same way as for  $\theta_3$  in (74). This yields

$$\Delta\theta_1 = \arccos\left(1 - \frac{1}{2r_1r_2}\sqrt{1 + \frac{1}{4m^2}}\right) \approx \arccos\left(1 - \frac{1}{2r_1r_2}\right). \quad (88)$$

However, the constraint also implies a limited width of  $r_1$ , depending on  $r_2$ . The maximum width  $\Delta r_1$  and mean  $\bar{r}_1$  were calculated in Sec. 4.2 to be

$$\Delta r_1 = r_2\sqrt{\frac{4}{m^2} + \frac{1}{m^4}}, \quad \bar{r}_1 = r_2\left(1 + \frac{1}{2m^2}\right). \quad (89)$$

This can be used to replace the  $\theta_1$  and  $r_1$  integrations in (75) in analogy to the case of  $\theta_3$  in (74), and one obtains

$$\begin{aligned} \frac{2}{3}\Delta P|_{3\text{-loop},st} &= i\frac{\Lambda^4}{576\lambda^2}e^4\frac{1}{(2\pi)^5}\int dr_2\frac{r_1^2r_2^4}{(r_1^2+m^2)(r_2^2+m^2)}\Delta r_1\sin(\Delta\theta_1/2)\Delta\theta_1 \\ &\quad \times \sin(\Delta\theta_3/2)\Delta\theta_3\left(132 + 72\frac{k^4}{m^4} + 12\frac{k^8}{m^8}\right)n_B'^2(r_1)n_B'^2(r_2). \end{aligned} \quad (90)$$

In (90)  $k$  is evaluated at  $\theta_1 = \Delta\theta_1/2$ ,  $r_1 = r_2(1 + 1/2m^2)$ , and the sum over energy-sign combinations has been dropped noting that  $\text{sgn}(p_1^0) = \text{sgn}(p_2^0)$ . This expression can be evaluated numerically. Working to first order in  $1/r_2$ , as in the diagonal case, however, renders the polynomial a constant since

$$k^4 = (p_1p_2)^2 \approx (r_1r_2(1 - \cos\bar{\theta}_1))^2 \approx r_1^2r_2^2\left(\frac{1}{2} \cdot \frac{1}{(2\sqrt{r_1r_2})^2}\right)^2 = \frac{1}{64}. \quad (91)$$

Approximating the mean  $\bar{r}_1 = r_2(1 + 1/(2m^2))$  by  $r_2$ , one finally obtains

$$\frac{2}{3}\Delta P|_{3\text{-loop},st} \approx i\frac{\Lambda^4}{\lambda^2}e^4C\int dr_2\frac{r_2^3}{(r_2^2+m^2)^2}n_B^4\left(2\pi\sqrt{\frac{r_2^2+m^2}{\lambda^3}}\right), \quad (92)$$

where we have introduced the constant

$$\begin{aligned} C &\equiv \frac{1}{2304}\frac{1}{(2\pi)^5}\sqrt{\frac{4}{m^2} + \frac{1}{m^4}}\left(132 + \frac{72}{64}\frac{1}{m^4} + \frac{3}{1024}\frac{1}{m^8}\right) \\ &\approx 6.5867 \cdot 10^{-7}. \end{aligned} \quad (93)$$

This integral is dominated by  $r_2 \ll \lambda$ . As was done for  $I_1$  in (83) and (84), we aim for a split of the integration

$$I_4 \equiv \int_0^\infty dx\frac{x^3}{(x^2+m^2)^2}n_B^4\left(2\pi\sqrt{\frac{x^2+m^2}{\lambda^3}}\right). \quad (94)$$

To be able to use (82) in one domain and the approximation

$$n_B(x) = \frac{1}{e^x - 1} \approx e^{-x}, \quad (95)$$

reliable for large  $x$ , in the other domain, we choose to split the integration at  $\hat{x} = \lambda^{3/2}/(2\pi)$  where the exponential becomes unity upon neglecting  $m$ . Using (82), we then find

$$\begin{aligned} I_4^{\hat{x}} &= \int_0^{\hat{x}} dx \frac{x^3}{(x^2 + m^2)^2} n_B^4 \left( 2\pi \sqrt{\frac{x^2 + m^2}{\lambda^3}} \right) \approx \frac{\lambda^6}{(2\pi)^4} \int_0^{\hat{x}} dx \frac{x^3}{(x^2 + m^2)^4} \\ &= \frac{\lambda^6}{(2\pi)^4} \frac{\hat{x}^6 + 3m^2 \hat{x}^4}{12m^4(m^2 + \hat{x}^2)^3} \\ &\approx \frac{\lambda^6}{(2\pi)^4} \frac{1}{12m^4(1 + \frac{m^2}{\hat{x}^2})^3} \approx \frac{\lambda^6}{(2\pi)^4} \frac{1}{12m^4} \end{aligned} \quad (96)$$

where in the final line we omitted terms of lower order in  $\lambda$ . Notice that this leading order is independent of the precise upper boundary  $\hat{x}$ : For any  $\hat{x} \propto \lambda^k$  with  $k > 0$  the first correction is proportional to  $\lambda^6 m^2 / \hat{x}^2 \propto \lambda^{6-2k}$ , and thus it is subleading. This already indicates the saturation of  $I_1$  well below  $\hat{x} = \lambda^{3/2}/(2\pi)$ . The other contribution to  $I_4$ ,  $I_4^\infty$  is estimated by virtue of (95) as

$$\begin{aligned} I_4^\infty &= \int_{\hat{x}}^\infty dx \frac{x^3}{(x^2 + m^2)^2} n_B^4 \left( 2\pi \sqrt{\frac{x^2 + m^2}{\lambda^3}} \right) \approx \int_{\hat{x}}^\infty dx \frac{1}{x} \left( e^{-2\pi \frac{x}{\lambda^{3/2}}} \right)^4 \\ &= \int_1^\infty dy y^{-1} e^{-4y} = \int_4^\infty d\bar{y} \bar{y}^{-1} e^{-\bar{y}} = \Gamma(0, 4) \end{aligned} \quad (97)$$

where, again,  $y \equiv 2\pi x / \lambda^{3/2}$ ,  $\bar{y} = 4y$ , and  $\Gamma(s, t)$  denotes the incomplete gamma function. We notice that  $I_4^\infty$  is constant in  $\lambda$ , and thus it can be dropped at high  $\lambda$ . Hence, we can recast (92) as

$$\frac{2}{3} \Delta P|_{3\text{-loop}, st} \approx i\Lambda^4 e^4 \frac{C}{(2\pi)^4} \frac{1}{12m^4} \lambda^4 \approx i\Lambda^4 \lambda^4 \cdot 2.2011 \cdot 10^{-12}. \quad (98)$$

The leading power in  $\lambda$  thus is identified to be four. We conclude that, concerning contributions to (75) from the integration range of large  $r_1$  and  $r_2$ , the diagonal channel's contribution is leading by a relative power of  $\lambda^{13-4} = \lambda^9$  in the high-temperature limit. Possible corrections from the integration domain of small radii can be accounted for in the Monte Carlo calculation and be compared to the approximation (98).

#### 4.4 Match of high- to low-temperature behaviour

In Figure 12 results for the 2PI three-loop pressure corrections  $1/3\Delta P|_{3\text{-loop}, ss}$  and  $2/3\Delta P|_{3\text{-loop}, st}$  are shown. (Recall that they add up to the full expression  $\Delta P|_{3\text{-loop}}$

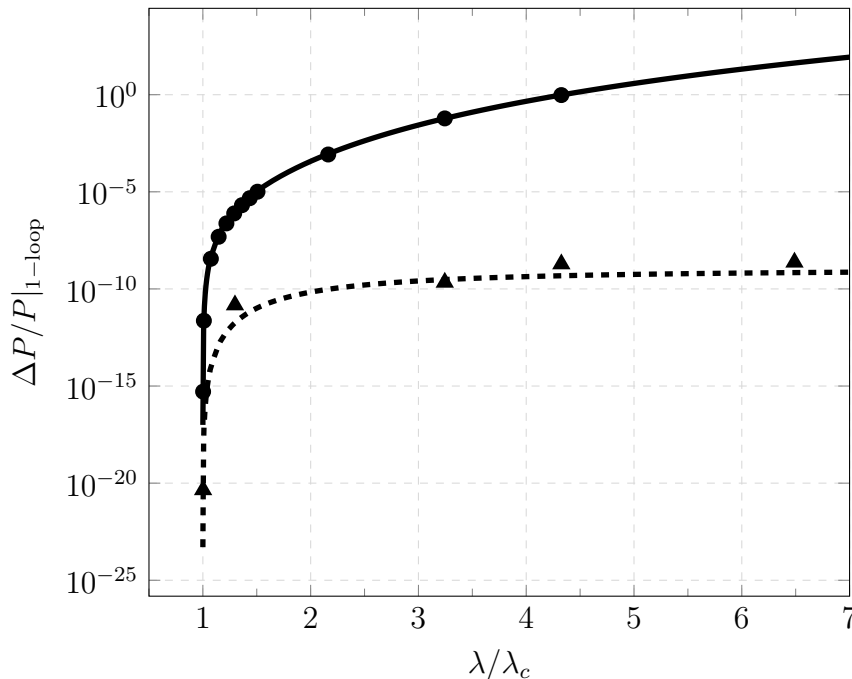


Figure 12: The moduli of the three-loop pressure corrections,  $1/3\Delta P|_{3\text{-loop},ss}$  (solid) and  $2/3\Delta P|_{3\text{-loop},st}$  (dashed), divided by the massive sector one-loop pressure  $P|_{1\text{-loop}}$ . The continuous curves represent the analytical high- $T$  expressions (78) and (90) while the dots and triangles are the respective  $ss$  and  $st$  Monte Carlo (MC) results. The MC results for the case  $st$  are less precise than those for  $ss$  at comparable running time because the additional constraint in the  $st$  case strongly decreases the MC hit rate.

in (42).) We compare Monte Carlo evaluations at low temperatures with the approximations derived in Sec. 4.3. The approximations are successful even for low values of  $\lambda$  in the vicinity of  $\lambda_c$ . With (78) we thus have extracted a simple and extremely well approximating expression for the 2PI three-loop which rapidly saturates into the power law of (86) with increasing  $\lambda$ .

Compared to the two-loop contribution  $\Delta P|_{2\text{-loop}}$  in Figure 8, whose ratio with the one-loop pressure  $P|_{1\text{-loop}}$  approaches zero at high temperatures, and compared to  $P|_{1\text{-loop}}$  in (37) itself, which increases with a Stefan-Boltzmann power of four, the 2PI three-loop diagram thus dominates at sufficiently high temperatures. However, in the vicinity of  $\lambda_c$ ,  $|\Delta P|_{3\text{-loop}}$  is found by Monte Carlo integration to be well suppressed with respect to  $P|_{1\text{-loop}}$  and  $|\Delta P|_{2\text{-loop}}$ . The transition regime, where the modulus of  $\Delta P|_{3\text{-loop}}$  becomes larger than the modulus of  $\Delta P|_{2\text{-loop}}$ , is shown in Figure 13. Notice that both,  $1/3\Delta P|_{3\text{-loop},ss}$  and  $2/3\Delta P|_{3\text{-loop},st}$ , are *purely imaginary*, see (78) and (90). This indicates that  $\Delta P|_{3\text{-loop}}$  radiative corrections to the free quasiparticle pressure cannot in general be interpreted as thermal. Rather, minute imaginary contributions, see Sec. 5, represent turbulent contributions to the pressure. This is not too surprising since they describe (minute) correlations between events induced

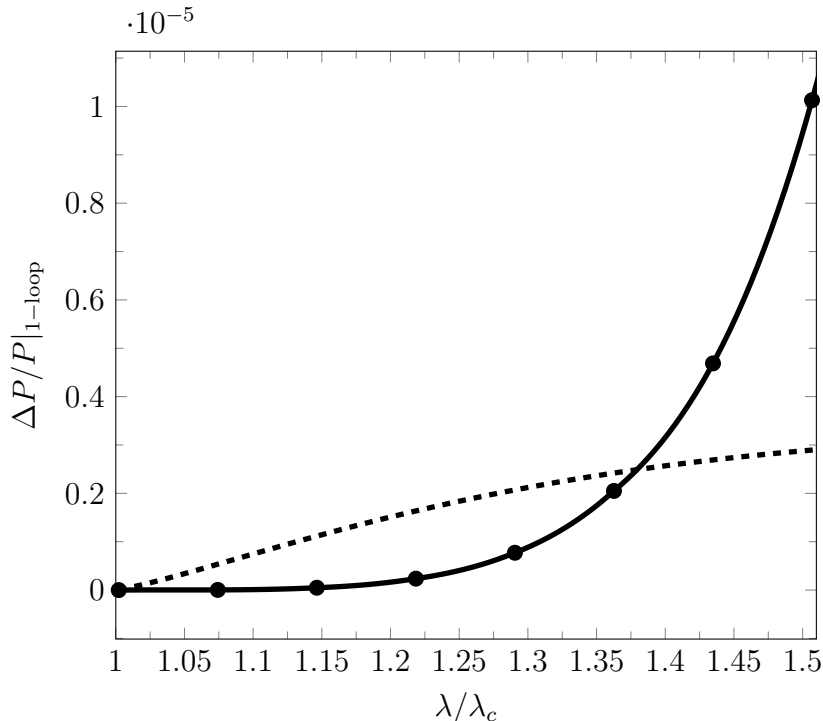


Figure 13: Monte Carlo results of  $\Delta P|_{3\text{-loop}}/P|_{1\text{-loop}}$  close to  $\lambda_c$  (dots). The solid line is a smooth interpolation of the latter while the dashed line represents  $\Delta P|_{2\text{-loop}}/P|_{1\text{-loop}}$ .

by (anti)caloron centers, and we know that such correlations induce isolated, screened monopole-antimonopole pairs [23] whose condensation at low temperatures implies a highly nonthermal Hagedorn transition [1].

As one would expect, the least-constrained channel combination by far dominates the 2PI three-loop pressure correction. Moreover, we have found the high-temperature limit of this contribution, namely (78) and its power law limit (86). The subleading contribution (90) is bounded relative to  $P|_{1\text{-loop}}$  since both are  $\propto \lambda^4$  as  $\lambda \rightarrow \infty$ .

The unboundedness with power thirteen of (86) as  $\lambda \rightarrow \infty$  calls for a reorganization of the loop expansion. In Sec. 2.3 we have shown that a class  $\mathcal{C}$  of diagrams with up to infinitely many loops exists where the loop integration is subject to a single constraint only just like in the diagonal configuration of the three-loop diagram. Resummation within  $\mathcal{C}$  actually resolves the unboundedness problem of the fixed loop order three as we will show in this section. Yet, we emphasise that comparing (86) and (98) demonstrates the suppressing strength of vertex constraints: The imposition of an additional constraint leads to a hierarchical drop in the scaling power at high temperatures. Namely, a power law  $\lambda^{13}$  reduces to a power law  $\lambda^4$ . This provides a certain amount of evidence that the consideration of the least constrained combinations are likely sufficient to identify contributions which make sense in a resummed form only.

## 5 Resummation of two-particle irreducible diagrams with dihedral symmetry

The Dyson-Schwinger equation for the resummed 4-vertex in scalar  $\lambda\varphi^4$ -theory without sources is given as [24]

$$\text{Resummed 4-vertex} = \text{Tree-level 4-vertex} + \text{Loop diagram 1} + \text{Loop diagram 2} + \text{Loop diagram 3}, \quad (99)$$

where dotted vertices are exact (subject to all-order resummations), internal lines denote resummed propagators, while external lines refer to arbitrary asymptotic states. There are also tree-level 4-vertices in the diagrams on the right hand side. It is required by the  $SU(2)$  algebra  $\mathfrak{su}(2)$  that only those two massive particles, which are oppositely charged w.r.t. the unbroken  $U(1)$  Cartan subalgebra  $\mathfrak{u}(1)$ , participate [1]. Considering this restriction, one can take over the diagrammatic equation from  $\lambda\varphi^4$  theory. We now demonstrate that (99) can be used to generate a well bounded loop expansion of the pressure by resummation. To this end, let us approximate the full propagator by its tree-level expression while assuming that the resummed 4-vertex  $\Gamma_{[4]}$  has the same tensorial structure as the tree-level 4-vertex, i.e.

$$\Gamma_{[4],abcd}^{\mu\nu\rho\sigma}|_i = f(\lambda, i)\Gamma_{[4],abcd}^{\mu\nu\rho\sigma}|_{i,\text{tree-level}} \quad (100)$$

where  $i = s, t, u$ , and  $f(\lambda, i)$  is a scalar function (form factor) encoding the dependences on invariant momentum transfer and temperature. Let us further truncate the DS equation after the second diagram on the right hand side of (99). This step cannot at present be justified rigorously but it appears plausible that, due to reduced symmetry, the third and fourth diagrams on the right hand side of (99) are much more constrained than the second one is. Under these assumptions, we may fix the color structure of this latter diagram since of the three options

$$\text{Diagram 1}, \quad \text{Diagram 2}, \quad \text{Diagram 3}, \quad (101)$$

where the 1 and 2 denote the respective massive directions in  $\mathfrak{su}(2)$ , only the first one is compatible with the vertex color structure. In this truncation, one can iterate the DS equation starting at tree-level on the right hand side. At each iteration step one

inserts the resummed vertex of the previous iteration as

$$\begin{aligned}
 & \text{Diagram with black dot (subscript 1)} = \text{Bare vertex} + \text{Vertex with loop and black dot} \\
 & \text{Diagram with black dot (subscript 2)} = \text{Bare vertex} + \text{Vertex with loop and black dot (subscript 1)} + \text{Vertex with two loops and black dot} \\
 & \text{Diagram with black dot (subscript 3)} = \text{Bare vertex} + \text{Vertex with loop and black dot} + \text{Vertex with two loops and black dot} + \text{Vertex with three loops and black dot} \\
 & \dots
 \end{aligned} \tag{102}$$

where the numbers in subscript denote the level of iteration at which the resummed vertex is evaluated. Therefore, the full resummation of the class of diagrams shown in (102) is encoded in the truncated version of the DS equation (99). Closing the legs into two (extra) loops to compare with two-loop and three-loop calculations transforms the truncated version of (99) into

$$\text{Diagram with black dot and two loops} = \text{Diagram with two loops} + \text{Diagram with two loops and black dot} . \tag{103}$$

Comparing with (102), this equation can be interpreted as the resummation of the class  $\mathcal{C}$  as defined in Sec. 2.3 since by iteration the chain

$$\text{Diagram with black dot and two loops} = \text{Diagram with two loops} + \text{Diagram with two loops and black dot} + \text{Diagram with two loops and black dot and triangle} + \text{Diagram with two loops and black dot and square} + \text{Diagram with two loops and black dot and pentagon} + \dots \tag{104}$$

is generated. In the high-temperature limit,  $f(\lambda, i)$  can be considered constant in momentum transfer,  $f(\lambda, i) \equiv f(\lambda)$  since the constraints demand that

$$|s|, |t|, |u| \leq |\phi|^2 = \frac{\Lambda^3}{2\pi T} \propto 1/T . \tag{105}$$

Thus  $f(\lambda)$  can be factored out in loop integrals, and the corresponding pressure contributions  $\Delta P|_{2\text{-loop}}$  and  $\Delta P|_{3\text{-loop}}$  imply

$$f(\lambda)\Delta P|_{2\text{-loop}} = \Delta P|_{2\text{-loop}} + f(\lambda)\Delta P|_{3\text{-loop}} . \tag{106}$$

Solving for  $f(\lambda)$  one arrives at

$$f(\lambda) = \frac{\Delta P|_{2\text{-loop}}}{\Delta P|_{2\text{-loop}} - \Delta P|_{3\text{-loop}}} . \tag{107}$$

The fact that  $\Delta P|_{3\text{-loop}}$  is imaginary while  $\Delta P|_{2\text{-loop}}$  is real ensures that no singularity is encountered as  $\lambda$  increases.

Let us compare this with the results of Sec. 4. For  $\lambda \gg \lambda_c$  the asymptotic form is  $\Delta P|_{3\text{-loop}} = 5.3 \cdot 10^{-20} i \Lambda^4 \lambda^{13}$  while for the two-loop diagram no analytic form was derived. Therefore, we will work with a fit to numerical data between  $\lambda = 200 = 14.42 \lambda_c$  and  $\lambda = 1000 = 72.10 \lambda_c$  which yields  $\Delta P|_{2\text{-loop}} = -5 \cdot 10^{-5} \Lambda^4 \lambda^{1.4}$ . Using this, the high-temperature behaviour of  $f(\lambda)$  is given as

$$\begin{aligned} f(\lambda) &= \frac{-5 \cdot 10^{-5} \lambda^{1.4}}{-5 \cdot 10^{-5} \lambda^{1.4} - 5.3 \cdot 10^{-20} i \lambda^{13}} \\ &= -0.94 \cdot 10^{15} i \lambda^{-11.6} \frac{1}{1 - 0.94 \cdot 10^{15} i \lambda^{-11.6}} \approx -0.94 \cdot 10^{15} i \lambda^{-11.6}. \end{aligned} \quad (108)$$

It follows that the resummed three-loop contribution (with both vertices resummed) becomes

$$\begin{aligned} f^2(\lambda) \Delta P|_{3\text{-loop}} &\approx (-0.94 \cdot 10^{15} i \lambda^{-11.6})^2 \cdot 5.3 \cdot 10^{-20} i \Lambda^4 \lambda^{13} \\ &= -4.7 \cdot 10^{10} i \Lambda^4 \lambda^{-10.2} \end{aligned} \quad (109)$$

which still is purely imaginary. Moreover, the resummed three-loop contribution is now sufficiently suppressed at high temperatures compared to  $P|_{1\text{-loop}}$ , as is the resummed two-loop contribution

$$\begin{aligned} f(\lambda) \Delta P|_{2\text{-loop}} &\approx -0.94 \cdot 10^{15} i \lambda^{-11.6} (-5 \cdot 10^{-5} \Lambda^4 \lambda^{1.4}) \\ &= 4.7 \cdot 10^{10} i \Lambda^4 \lambda^{-10.2}. \end{aligned} \quad (110)$$

In fact, it is rigorously guaranteed that the leading orders in  $\lambda$  of the resummed three-loop and two-loop diagrams (109) and (110), respectively, cancel. This is because

$$f(\lambda) \approx -\frac{\Delta P|_{2\text{-loop}}}{\Delta P|_{3\text{-loop}}} \quad (111)$$

such that

$$\begin{aligned} f^2(\lambda) \Delta P|_{3\text{-loop}} &= \frac{(\Delta P|_{2\text{-loop}})^2}{\Delta P|_{3\text{-loop}}} \\ f(\lambda) \Delta P|_{2\text{-loop}} &= -\frac{(\Delta P|_{2\text{-loop}})^2}{\Delta P|_{3\text{-loop}}}. \end{aligned} \quad (112)$$

Amusingly, if we pretend that (107) can be extended down to  $\lambda_c$ , we can infer from  $|\Delta P|_{2\text{-loop}} \gg |\Delta P|_{3\text{-loop}}$  that  $f(\lambda) \approx 1$  at low temperatures. This would mean that in the vicinity of  $\lambda_c$  no modification of the bare 4-vertex occurs. Let us again comment on the imaginary nature of the resummed two-loop and three-loop corrections to the pressure. (The fact that their leading powers in  $\lambda$  cancel does not necessarily extend to subleading powers.) The  $P|_{1\text{-loop}}$  was derived demanding thermodynamical selfconsistency at one-loop level. The impossibility to extend thermodynamical selfconsistency beyond one-loop order is reflected by small (and thus well controlled) imaginary and thus non-thermal corrections to the pressure which arise upon resummation of 2PI diagrams with dihedral symmetry.

## 6 Summary, Conclusions, and Outlook

In the present work we have readdressed the loop expansion in the deconfining phase of SU(2) Yang-Mills thermodynamics. Upon analysing the constraining power imposed by 4-vertices on loop integrations in the massive sector, arising from kinematic restriction on momentum transfer due to the principle unresolvability of (anti)caloron centers, in terms of allowed energy-sign and scattering-channel combinations, we have found that there is an infinite class  $\mathcal{C}$  of 2PI diagrams, exhibiting dihedral symmetry, with non-vanishing support of their loop integrations. The expectation that the loop expansion terminates at a finite 2PI loop order [22] thus is refuted. Upon further analysis of the first member of class  $\mathcal{C}$  we arrive at the interesting situation that, for temperatures not far above the critical temperature of the deconfining-preconfining phase transition [1], a hierarchical suppression of three-loop vs. two-loop vs. one-loop is observed while the modulus of the three-loop pressure correction rises by a high power at high temperatures, and thus is unbounded compared to lower loop orders. Based on the expectation that *fixed* loop orders should represent small corrections to the a priori estimate posited by the thermal ground state and its free quasiparticle excitations this would represent a disaster.

However, there definitely is a way out of this apparent dilemma. Namely, a formal resummation of *all* diagrams in class  $\mathcal{C}$  by virtue of the truncated Dyson-Schwinger equation for the vertex yields an extremely well bounded high-temperature dependence which is analytically connected to the low-temperature situation. Moreover, we show that this resummed correction to the free quasiparticle pressure is *imaginary* at high temperatures, and thus, albeit strongly suppressed, not interpretable as a thermal effect. The leading (highly negative) powers in two-loop and 2PI three-loop corrections to the pressure, when subjected to resummed 4-vertices, cancel, however. There is an interesting geometric interpretation of (small) imaginary radiative corrections in thermodynamical quantities. Namely, the a priori estimate of the thermal ground state assumes that the dense packing of ball-shaped (anti)caloron centers yields a spatially homogeneous situation. However, there are packing voids violating this assumption, and we may attribute the implied correction to spatial homogeneity to the presence of turbulence-related imaginary contributions in the loop expansion.

It will be interesting to analyse further the less symmetric five- and six-loop diagrams of Secs. 2.2.4 and 2.2.5 in terms of their high-temperature behaviour. We expect that they are much more constrained, likely so much that resummations no longer are required.

## Acknowledgments

We thank the Centre National de la Recherche Scientifique (CNRS) for the funding of RH during a one-month stay at INLN (Nice) in August-September 2016 where, among other projects, this work was conceived, and IB would like to thank ITP of the University of Heidelberg to fund his stay at INLN during a part of this period.

## A Derivation of equation (42)

By rescaling loop momenta with  $|\phi|$  and considering overall four-momentum conservation, one shows in a straightforward way that a bubble diagram with  $n$  4-vertices generates the following schematic contribution to the pressure

$$\frac{I_n}{(4\pi)^4 \delta^{(4)}(0)} = |\phi|^{4 \cdot 2n} |\phi|^{-4 \cdot (n-1)} |\phi|^{-2 \cdot 2n} \tilde{I}_n = |\phi|^4 \tilde{I}_n = \left| \sqrt{\frac{\Lambda^2}{\lambda}} \right|^4 \tilde{I}_n = \frac{\Lambda^4}{\lambda^2} \tilde{I}_n, \quad (113)$$

where  $I_n$  represents the loop integral arising by application of Feynman rules, and  $\tilde{I}_n$  is the according integral in dimensionless integration variables. Recall that  $\lambda = 2\pi T/\Lambda$ . Equation (113) makes explicit that the mass dimension of pressure is four.

Straightforward application of the Feynman rules [1] to the diagram in Figure 9 yields (dimensionless integration variables and  $m$ )

$$\begin{aligned} \Delta P|_{3\text{-loop}} &= \frac{\Lambda^4}{96i\lambda^2} \int \frac{d^4 p_1 d^4 p_2 d^4 p_3 d^4 p_4}{(2\pi)^{16}} (-ie^2)^2 (2\pi)^4 \delta^{(4)}(-p_1 - p_4 + p_3 + p_2) \\ &\quad \times \zeta_{a_1 b_1 c_1 d_1}^{\mu_1 \nu_1 \rho_1 \sigma_1} \zeta_{a_2 b_2 c_2 d_2}^{\mu_2 \nu_2 \rho_2 \sigma_2} (-2\pi)^4 \delta_{c_2 a_1} \delta_{c_1 a_2} \delta_{d_1 b_2} \delta_{d_2 b_1} \tilde{D}_{\rho_2 \mu_1}(p_1) \tilde{D}_{\rho_1 \mu_2}(p_3) \\ &\quad \times \tilde{D}_{\sigma_1 \nu_2}(p_2) \tilde{D}_{\sigma_2 \nu_1}(p_4) \delta(p_1^2 - m^2) \delta(p_2^2 - m^2) \delta(p_3^2 - m^2) \delta(p_4^2 - m^2) \\ &\quad \times n'_B(|\mathbf{p}_1|) n'_B(|\mathbf{p}_2|) n'_B(|\mathbf{p}_3|) n'_B(|\mathbf{p}_4|), \end{aligned} \quad (114)$$

where  $n'_B(|\mathbf{p}|) \equiv n_B(2\pi\sqrt{|\mathbf{p}|^2 + m^2}/\lambda^{3/2})$  is introduced as a shorthand. The tensor structure  $\zeta_{abcd}^{\mu\nu\rho\sigma}$  is defined as

$$\zeta_{abcd}^{\mu\nu\rho\sigma} \equiv \epsilon_{fab} \epsilon_{fcd} (g^{\mu\rho} g^{\nu\sigma} - g^{\mu\sigma} g^{\nu\rho}) + \quad (115)$$

$$\epsilon_{fac} \epsilon_{fdb} (g^{\mu\sigma} g^{\rho\nu} - g^{\mu\nu} g^{\rho\sigma}) + \epsilon_{fad} \epsilon_{fbc} (g^{\mu\nu} g^{\sigma\rho} - g^{\mu\rho} g^{\sigma\nu}), \quad (116)$$

where  $\epsilon_{abc}$  denotes the Levi-Civita symbol, and the propagator's tensor  $\tilde{D}_{\mu\nu}(p)$  reads

$$\tilde{D}_{\mu\nu}(p) = g_{\mu\nu} - \frac{p_\mu p_\nu}{m^2}. \quad (117)$$

First, we sum over color (latin) indices, ranging from 1 to 2 (massive sector only). The contractions involving Kronecker symbols yield

$$\begin{aligned} &\frac{\Lambda^4}{96i\lambda^2} \int \frac{d^4 p_1 d^4 p_2 d^4 p_3 d^4 p_4}{(2\pi)^{16}} (-ie^2)^2 (2\pi)^4 \delta^{(4)}(-p_1 - p_4 + p_3 + p_2) \zeta_{abcd}^{\mu_1 \nu_1 \rho_1 \sigma_1} \zeta_{cdab}^{\mu_2 \nu_2 \rho_2 \sigma_2} \\ &\quad \times (-2\pi)^4 \tilde{D}_{\rho_2 \mu_1}(p_1) \tilde{D}_{\rho_1 \mu_2}(p_3) \tilde{D}_{\sigma_1 \nu_2}(p_2) \tilde{D}_{\sigma_2 \nu_1}(p_4) \delta(p_1^2 - m^2) \delta(p_2^2 - m^2) \\ &\quad \times \delta(p_3^2 - m^2) \delta(p_4^2 - m^2) n'_B(|\mathbf{p}_1|) n'_B(|\mathbf{p}_2|) n'_B(|\mathbf{p}_3|) n'_B(|\mathbf{p}_4|) \end{aligned} \quad (118)$$

with a relabelling  $a_1, b_1, c_1, d_1 \rightarrow a, b, c, d$ . Because of the restriction to the massive sector, we have  $\epsilon_{fmn} = \epsilon_{3mn} = \epsilon_{mn}$  for  $m, n = 1, 2$ , and one can write

$$\begin{aligned} &\zeta_{abcd}^{\mu_1 \nu_1 \rho_1 \sigma_1} \zeta_{cdab}^{\mu_2 \nu_2 \rho_2 \sigma_2} \\ &= [\epsilon_{ab} \epsilon_{cd} G_1^A + \epsilon_{ac} \epsilon_{db} G_1^B + \epsilon_{ad} \epsilon_{bc} G_1^C] \cdot [\epsilon_{cd} \epsilon_{ab} G_2^A + \epsilon_{ca} \epsilon_{bd} G_2^B + \epsilon_{cb} \epsilon_{da} G_2^C] \\ &= 4 (G_1^A G_2^A + G_1^B G_2^B + G_1^C G_2^C) \\ &\quad - 2 (G_1^A G_2^B + G_1^A G_2^C + G_1^B G_2^A + G_1^B G_2^C + G_1^C G_2^A + G_1^C G_2^B), \end{aligned} \quad (119)$$

where the superindices  $A$ ,  $B$ , and  $C$  encode the Lorentz structure as

$$\begin{aligned}
G_i^A &\equiv g^{\mu_i \rho_i} g^{\nu_i \sigma_i} - g^{\mu_i \sigma_i} g^{\nu_i \rho_i} \\
G_i^B &\equiv g^{\mu_i \sigma_i} g^{\rho_i \nu_i} - g^{\mu_i \nu_i} g^{\rho_i \sigma_i} \\
G_i^C &\equiv g^{\mu_i \nu_i} g^{\sigma_i \rho_i} - g^{\mu_i \rho_i} g^{\sigma_i \nu_i} .
\end{aligned} \tag{120}$$

Relabelling  $\mu_1, \nu_1, \rho_1, \sigma_1 \rightarrow \mu, \nu, \rho, \sigma$  and  $\mu_2, \nu_2, \rho_2, \sigma_2 \rightarrow \bar{\mu}, \bar{\nu}, \bar{\rho}, \bar{\sigma}$ , (119) evaluates to

$$\begin{aligned}
&12 (g^{\mu\rho} g^{\nu\sigma} g^{\bar{\mu}\bar{\rho}} g^{\bar{\nu}\bar{\sigma}} + g^{\mu\sigma} g^{\nu\rho} g^{\bar{\mu}\bar{\sigma}} g^{\bar{\nu}\bar{\rho}} + g^{\mu\nu} g^{\rho\sigma} g^{\bar{\mu}\bar{\nu}} g^{\bar{\rho}\bar{\sigma}}) \\
&\quad - 6 (g^{\mu\rho} g^{\nu\sigma} g^{\bar{\mu}\bar{\sigma}} g^{\bar{\nu}\bar{\rho}} + g^{\mu\sigma} g^{\nu\rho} g^{\bar{\mu}\bar{\rho}} g^{\bar{\nu}\bar{\sigma}} + g^{\mu\sigma} g^{\nu\rho} g^{\bar{\mu}\bar{\nu}} g^{\bar{\rho}\bar{\sigma}} \\
&\quad\quad + g^{\mu\nu} g^{\rho\sigma} g^{\bar{\mu}\bar{\sigma}} g^{\bar{\nu}\bar{\rho}} + g^{\mu\nu} g^{\rho\sigma} g^{\bar{\mu}\bar{\rho}} g^{\bar{\nu}\bar{\sigma}} + g^{\mu\rho} g^{\nu\sigma} g^{\bar{\mu}\bar{\nu}} g^{\bar{\rho}\bar{\sigma}}) . \tag{121}
\end{aligned}$$

The entire integral with contractions reduced to scalar products, upon execution of the  $p_4$  integration in (118) by virtue of the delta function  $\delta^{(4)}$ , and exploiting  $p_i^2 = m^2$  due to delta functions  $\delta$ , is computed to be

$$\begin{aligned}
&\Delta P|_{3\text{-loop}} \\
&= i \frac{\Lambda^4}{96\lambda^2} e^4 (2\pi)^4 \int \frac{d^4 p_1 d^4 p_2 d^4 p_3}{(2\pi)^{12}} \left\{ 144 \right. \\
&\quad - 12 \frac{1}{m^4} [(p_1 p_2)^2 + (p_1 p_3)^2 + (p_1 p_4)^2 + (p_2 p_3)^2 + (p_2 p_4)^2 + (p_3 p_4)^2] \\
&\quad + 36 \frac{1}{m^6} [(p_1 p_2)(p_1 p_3)(p_2 p_3) + (p_1 p_2)(p_1 p_4)(p_2 p_4) \\
&\quad\quad + (p_1 p_3)(p_1 p_4)(p_3 p_4) + (p_2 p_3)(p_2 p_4)(p_3 p_4)] \\
&\quad + 12 \frac{1}{m^8} [(p_1 p_2)^2 (p_3 p_4)^2 + (p_1 p_3)^2 (p_2 p_4)^2 + (p_1 p_4)^2 (p_2 p_3)^2 \\
&\quad\quad - (p_1 p_2)(p_1 p_3)(p_2 p_4)(p_3 p_4) - (p_1 p_2)(p_1 p_4)(p_2 p_3)(p_3 p_4) \\
&\quad\quad\quad \left. - (p_1 p_3)(p_1 p_4)(p_2 p_3)(p_2 p_4)] \right\} \\
&\quad \times \delta(p_1^2 - m^2) \delta(p_2^2 - m^2) \delta(p_3^2 - m^2) \delta(p_4^2 - m^2) \\
&\quad \times n'_B(|\mathbf{p}_1|) n'_B(|\mathbf{p}_2|) n'_B(|\mathbf{p}_3|) n'_B(|\mathbf{p}_4|) , \tag{122}
\end{aligned}$$

where  $p_4 = p_2 + p_3 - p_1$ . The polynomial in braced brackets is denoted by  $P(\{p_i\})$  in (47).

In a next step the delta functions  $\delta$  are integrated away, introducing a sum over 16 possible sign combinations which can be reduced to 8 inequivalent combinations: We make the convention that the sign of  $p_1^0$  is plus. Vertex constraints restrict these configurations further, see (7), (8), and (9). The ‘‘diagonal’’ channels  $ss$ ,  $tt$ , and  $uu$  give equal results since the integrand is symmetric under permutations of  $p_1$ ,  $p_2$ ,  $p_3$  and  $p_4$  and under inversion  $p_i \rightarrow -p_i$ . The same is true for the ‘‘off-diagonal’’ channels  $st$ ,  $su$ , and  $tu$ . Considering that each of the two vertices decomposes into equally weighted  $s$ ,

$u$ , and  $t$  contributions, there are nine copies of the integral  $\Delta P|_{3\text{-loop}}$ , each weighted by  $1/9$ . The diagonal channels add up to  $1/3\Delta P|_{3\text{-loop,ss}}$  while the off-diagonal channels add up to  $2/3\Delta P|_{3\text{-loop,st}}$ . Namely, recalling the results of [subsection 2.2.2](#), one notes that off-diagonal channels reduce to one allowed configuration

$$p_1^0 > 0, \quad p_2^0 > 0, \quad p_3^0 < 0, \quad p_4^0 < 0 \quad (st\text{-channel}) \quad (123)$$

and that the diagonal channels admit two configurations,

$$\begin{aligned} p_1^0 > 0, \quad p_2^0 > 0, \quad p_3^0 < 0, \quad p_4^0 < 0 \quad \text{or} \\ p_1^0 > 0, \quad p_2^0 < 0, \quad p_3^0 > 0, \quad p_4^0 < 0 \quad (ss\text{-channel}). \end{aligned} \quad (124)$$

With the following parametrisation  $\mathbf{p}_i \equiv r_i(\sin \theta_i \cos \varphi_i, \sin \theta_i \sin \varphi_i, \cos \theta_i)^T$  for  $i = 1, 2, 3$  and appealing to overall rotational symmetry the integrations over angles  $\theta_2, \varphi_2$ , and  $\varphi_3$  can be performed trivially. Finally, one arrives at

$$\begin{aligned} \Delta P|_{3\text{-loop}} &= i \frac{\Lambda^4}{96\lambda^2} e^4 \frac{1}{(2\pi)^8} \sum_{\text{signs}} \int d^3 p_1 d^3 p_2 d^3 p_3 P(\{p_i\}) \\ &\quad \times \delta \left( p_4^0 \mp \sqrt{r_4^2 + m^2} \right) \frac{n'_B(r_1)n'_B(r_2)n'_B(r_3)n'_B(r_4)}{8|p_1^0 p_2^0 p_3^0 p_4^0|} \\ &= i \frac{\Lambda^4}{96\lambda^2} e^4 \frac{1}{(2\pi)^8} \sum_{\text{signs}} \left( \int d\Omega_1 dr_1 \cdot 4\pi \int dr_2 \cdot 2\pi \int_0^\pi d\theta_3 \int dr_3 \right) \\ &\quad \times r_1^2 r_2^2 r_3^2 \sin \theta_3 P(\{p_i\}) \delta \left( p_4^0 \mp \sqrt{r_4^2 + m^2} \right) \frac{n'_B(r_1)n'_B(r_2)n'_B(r_3)n'_B(r_4)}{8|p_1^0 p_2^0 p_3^0 p_4^0|} \\ &= i \frac{\Lambda^4}{48\lambda^2} e^4 \frac{1}{(2\pi)^6} \sum_{\text{signs}} \int d\theta_1 d\varphi_1 dr_1 dr_2 d\theta_3 \sum_{\{r_3\}} r_1^2 r_2^2 r_3^2 \sin \theta_1 \sin \theta_3 \\ &\quad \times P(\{p_i\}) \frac{n'_B(r_1)n'_B(r_2)n'_B(r_3)n'_B(r_4)}{8|p_1^0 p_2^0 p_3^0 p_4^0|}, \end{aligned} \quad (125)$$

where  $|p_i^0| = \sqrt{r_i^2 + m^2}$ , and in the last step the  $r_3$  integration is executed by summing over solutions in  $r_3$  of

$$\begin{aligned} \text{sgn}(p_2^0) \sqrt{r_2^2 + m^2} + \text{sgn}(p_3^0) \sqrt{r_3^2 + m^2} - \sqrt{r_1^2 + m^2} &= \text{sgn}(p_4^0) [r_1^2 + r_2^2 + r_3^2 \\ &\quad - 2r_1 r_2 \cos \theta_1 - r_1 r_3 (\sin \varphi_1 \sin \theta_1 \sin \theta_3 + \cos \theta_1 \cos \theta_3) + r_2 r_3 \cos \theta_3 + m^2]^{1/2}. \end{aligned} \quad (126)$$

## References

- [1] R. Hofmann. *The thermodynamics of quantum Yang-Mills theory*. World Scientific Publishing Company, second edition, 2016.

- [2] E.V. Shuryak. *Sov.Phys.JETP*, 47:212, 1978.
- [3] E. Braten and R. Pisarski. *Phys.Rev.Lett.*, 64:1338, 1990.
- [4] E. Braten and R. Pisarski. *Nucl.Phys.B*, 337:569, 1990.
- [5] J. Frenkel and J.C. Taylor. *Nucl.Phys.B*, 334:199, 1990.
- [6] P. Arnold and Ch. Zhai. *Phys.Rev.D*, 50:7603, 1994.
- [7] Ch. Zhai and B. Kastening. *Phys.Rev.D*, 52:7232, 1994.
- [8] E. Braten and A. Nieto. *Phys.Rev.D*, 53:3421, 1996.
- [9] A.D. Linde. *Phys.Lett.B*, 96(3):289–292, 1980.
- [10] K. Kajantie, M. Laine, K. Rummukainen, and Y. Schroeder. *Phys.Rev.D*, 67:105008, 2003, arXiv:hep-ph/0211321.
- [11] I. Bischer, T. Grandou, and R. Hofmann. work in progress. 2017.
- [12] B. J. Harrington and H. K. Shepard. *Phys.Rev.D*, 17:2122–2125, Apr 1978.
- [13] R. Hofmann. *Entropy*, 18(19)(1):310, 2016, arXiv:1604.05136.
- [14] T. S. Evans. What is being calculated in thermal field theory. *Proc. of “Particle physics and cosmology”, Lake Louise*, page 343, 1994.
- [15] S. J. Brodsky and P. Hoyer. *Phys.Rev.D*, 83:045026, 2010, arXiv:1009.2313.
- [16] M. Schwarz, R. Hofmann, and F. Giacosa. *Int.J.Mod.Phys.A*, 22:1213–1238, 2007, arXiv:hep-th/0603078.
- [17] D. Kaviani and R. Hofmann. *Mod.Phys.Lett.A*, 22:2343–2352, 2007, arXiv:0704.3326.
- [18] N. Krasowski and R. Hofmann. *Ann.Phys.*, 347:287–308, 2014, arXiv:1301.4716.
- [19] H. Kleinert, A. Pelster, B. Kastening, and M. Bachmann. *Phys.Rev.E*, 62:1537–1559, 2000, arXiv:hep-th/9907168.
- [20] I. Bischer. *Master thesis*. Universität Heidelberg, first edition, 2017.
- [21] U. Herbst, R. Hofmann, and J. Rohrer. *Acta Phys.Polon.B*, 36:881–904, 2004, arXiv:hep-th/0410187.
- [22] R. Hofmann. *Braz.J.Phys.*, 42:110–119, 2006, arXiv:hep-th/0609033.
- [23] J. Ludescher et al. *Ann.d.Phys.*, 19:102–120, 2010, arXiv:0812.1858.
- [24] E. S. Swanson. *AIP Conf.Proc.*, 1296:75–121, 2010, arXiv:1008.4337.